

www.acsnano.org

Porous Silicon-Based Nanomedicine for Simultaneous Management of Joint Inflammation and Bone Erosion in Rheumatoid Arthritis

Moonkyoung Jeong, Yuna Jung, Junyong Yoon, Jinyoung Kang, Seo Hyeon Lee, Woojin Back, Hyoyeon Kim, Michael J. Sailor, Dokyoung Kim,* and Ji-Ho Park*



Downloaded via UNIV OF CALIFORNIA SAN DIEGO on November 8, 2022 at 02:37:20 (UTC). See https://pubs.acs.org/sharingguidelines for options on how to legitimately share published articles.

Cite This: ACS Nano 2022, 16, 16118-16132



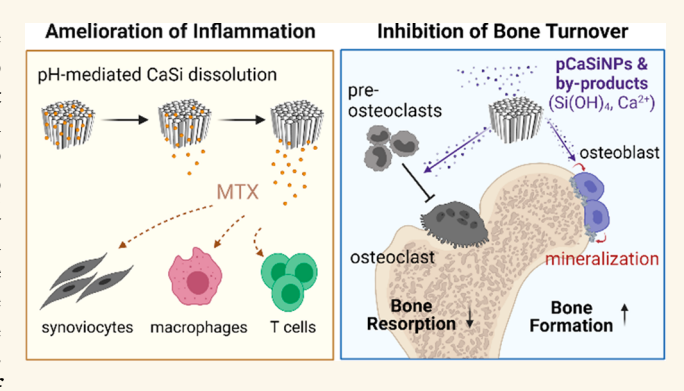
ACCESS

Metrics & More

Article Recommendations

si Supporting Information

ABSTRACT: The lack of drugs that target both disease progression and tissue preservation makes it difficult to effectively manage rheumatoid arthritis (RA). Here, we report a porous silicon-based nanomedicine that efficiently delivers an antirheumatic drug to inflamed synovium while degrading into bone-remodeling products. Methotrexate (MTX) is loaded into the porous silicon nanoparticles using a calcium silicate based condenser chemistry. The calcium silicate-porous silicon nanoparticle constructs (pCaSiNPs) degrade and release the drug preferentially in an inflammatory environment. The biodegradation products of the pCaSiNP drug carrier are orthosilicic acid and calcium ions, which exhibit immunomodulatory and antiresorptive effects. In a mouse model of



collagen-induced arthritis, systemically administered MTX-loaded pCaSiNPs accumulate in the inflamed joints and ameliorate the progression of RA at both early and established stages of the disease. The disease state readouts show that the combination is more effective than the monotherapies.

KEYWORDS: bone regeneration, drug delivery, methotrexate, porous silicon nanoparticle, rheumatoid arthritis

INTRODUCTION

Rheumatoid arthritis (RA) is an autoimmune disease that is characterized by local joint inflammation and articular damage. Despite significant efforts to identify RA pathologies and develop RA therapeutics, treatments providing sustained or complete remission remain elusive. While several drugs are clinically approved to treat RA patients, they provide limited remission in only a few patients and are associated with various side effects. Glucocorticoids, such as prednisolone and dexamethasone, are substantially effective treatments for acute RA; however, their long-term use is avoided due to severe side effects, including osteoporosis, lipid abnormalities, and adrenal suppression.² Disease-modifying antirheumatic drugs (DMARDs) are commonly used to treat RA patients. This class of drugs slows disease progression by interfering with inflammatory cascades in various immune cells, and they generally display less serious side effects compared with other drugs. DMARDs can be synthetic small molecules or biologics. Methotrexate (MTX) is a synthetic DMARD that is currently

the most strongly recommended drug for RA treatment according to the American College of Rheumatology (ACR) guidelines.3 It acts on various types of inflammatory immune cells. In particular, MTX sensitizes effector T cells to apoptosis by inhibiting dihydrofolate reductase and it downregulates proinflammatory functions in T cells and fibroblast-like synoviocytes (FLSs), which are fibroblasts of the synovial lining, by inhibiting nuclear factor-κB (NF-κB) activity.⁴ However, repeated administration of MTX is associated with gastrointestinal toxicity, hepatotoxicity, nephrotoxicity, and osteoporosis.^{5–8}

Received: May 8, 2022 Accepted: October 6, 2022 Published: October 10, 2022

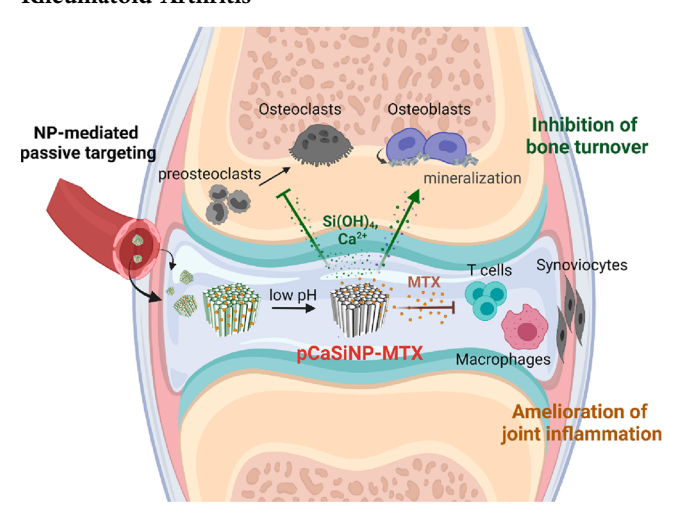




The progression of RA increases the risk of developing osteoporosis. For instance, abnormal proliferation of FLSs and osteoclasts causes bone erosion in the inflammatory environment of the RA synovium.9 To counteract this, teriparatide (anabolic agent)¹⁰ and denosumab [an antibody against the receptor activator of NF-kB ligand (anti-RANKL)]11 have been used to stimulate bone formation in RA patients. However, teriparatide treatment has side effects, such as osteosarcoma and calciphylaxis, 12,13 whereas denosumab monotherapy has negligible effects on disease modification¹⁴ and increases the individual risk of adverse events including eczema, allergic reactions, skin infections, hypocalcemia, and osteonecrosis of the jaw. 15 Clinical trials of a combination therapy of denosumab with MTX successfully inhibited bone erosion, 16 though it failed to show an additive antiinflammatory effect. Moreover, the need for frequent infusions and extended medication schedules for these two therapies engenders patient compliance issues. The motivation for this present study was to overcome the disadvantages of current antirheumatic and antiresorptive treatments by developing a combination therapy that could more effectively synergize its action against these two targets in RA. We focused on a nanoparticle delivery platform composed of silicon and calcium-based components.

Nanoparticle formulations have been extensively investigated because of their efficient delivery of drugs to disease environments with a leaky vasculature, such as tumors and inflamed joints. 17,18 The present approach uses porous silicon nanoparticles (pSiNPs), which have demonstrated a high capacity for the loading of a variety of drugs and good biodegradability.¹⁹ They are synthesized by first generating a mesoporous silicon film via electrochemical anodization of silicon wafers, followed by ultrasonic fracturing of the film to prepare the nanoparticles.²⁰ The electrochemical processing conditions allow for precise tuning of the mesoporous nanostructure,²¹ and efficient loading of antirheumatic drugs with poor water solubility such as MTX²² has been demonstrated. The silicon-based composition of the nanoparticles is also attractive for the purposes of bone regeneration.^{23,24} The silicon and silicon oxide species present in pSiNPs readily decompose in aqueous environments to generate orthosilicic acid (OSA). At physiologic pH values, OSA primarily exists as Si(OH)₄, which is the bioavailable form of silicon naturally present in mammalian tissues.²⁵ Recent studies have demonstrated the beneficial effects of OSA on bone regeneration in vitro and in vivo, as it inhibits osteoclastogenesis and stimulates bone mineralization. 26-28 In addition, the silicon oxides present on the surface of pSiNPs readily react with excess calcium ion (Ca²⁺) to form a calcium silicate (Ca₂SiO₄) layer, which degrades into a major component involved in bone mineralization. ^{29–31} This calcium silicate coating enables the stable loading of drugs in the porous nanostructure and their preferential release in acidic disease microenvironments.³² Here, we introduce calcium silicate coated pSiNPs (pCaSiNPs) that can efficiently deliver MTX to the inflamed synovium and dissolve to produce the antiresorptive substances orthosilicic acid and calcium ion byproducts that exhibit bone-remodeling effects. We find that this combination achieves synergistic antirheumatic effects by simultaneously managing inflammation and bone turnover (Scheme 1).

Scheme 1. Schematic Representation of Mode of Action of the MTX-Loaded pCaSiNP (pCaSiNP-MTX) in Rheumatoid Arthritis



RESULTS AND DISCUSSION

Preparation and Characterization of pSiNPs and pCaSiNPs. The pSiNPs were prepared following a previously developed "perforated etch" protocol.³³ In brief, highly doped p++2-type silicon wafers were electrochemically anodized to form a porous silicon multilayer, which was removed from the substrate and subjected to ultrasonic fracturing, and the resulting pSiNPs were purified and isolated by centrifugation steps (Figure S1), which generated nanosized particles with a well-defined mesoporous nanostructure (Figure 1A). Scanning electron microscopy (SEM) and Barrett-Joyner-Halenda (BJH) analysis of cryogenic nitrogen adsorption data indicated pore sizes in the range of 13-15 nm (Figure 1A and Figure S2). The average hydrodynamic size and surface charge, as measured by dynamic light scattering (DLS), were 245 \pm 92 nm and -23.1 ± 7.6 mV, respectively (Table 1). These preparation conditions were optimized to maximize drug loading and calcium silicate content in the final pCaSiNP preparations. The calcium silicate layer was deposited by slow oxidation of the pSiNPs in water to form silicon oxide, followed by incubation in a highly concentrated aqueous solution of calcium(II) ions as previously described.³¹ We observed that the pores of the pCaSiNPs were partially closed in the SEM images, implying that a calcium silicate coating was formed on the surface of the pSiNPs (Figure 1B). The average hydrodynamic size and surface charge of the resulting pCaSiNPs had increased to 262 \pm 62 nm and -13.0 \pm 7.1 mV, respectively, following calcium silicate coating (Table 1).

While pSiNPs degrade into OSA under physiological conditions, their biodegradation can be regulated by surface coatings. The vitro dynamic light scattering measurements indicated that in a solution of normal physiological pH (pH 7.4, maintained at 37 °C), pSiNPs degraded to 10% of their initial value after 0.5 h of incubation. In contrast, pCaSiNPs required a substantially longer time (4 h of incubation) to reach the same level of degradation (Figure 1C). The calcium silicate layer on the pCaSiNPs dissolved more rapidly in an acidic solution that mimicked an inflammatory environment (pH 6.0, maintained at 37 °C) compared to more normal physiological conditions (pH 7.4, maintained at 37 °C). Thus, inductively coupled plasma optical emission spectrometry

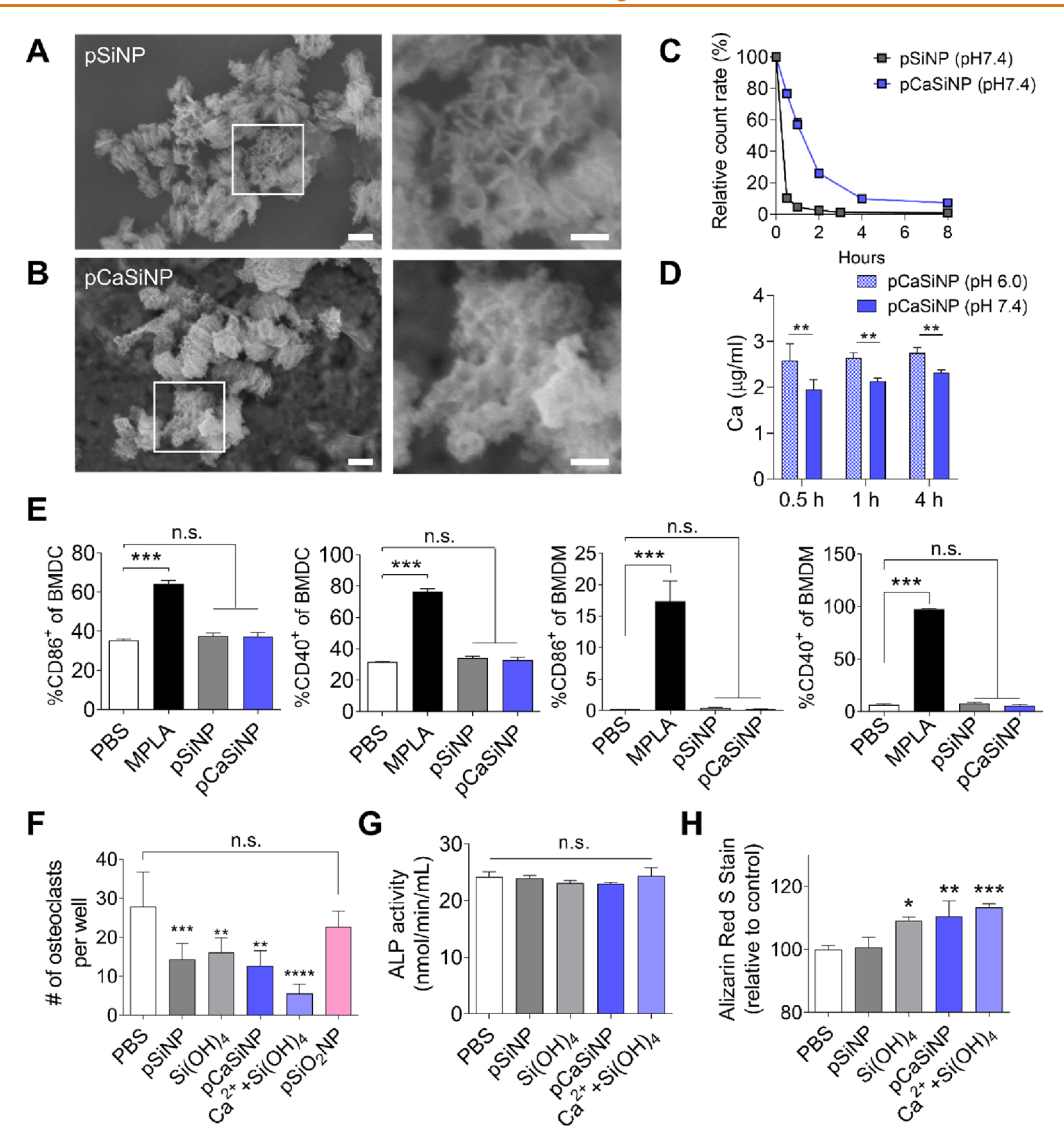


Figure 1. Physicochemical and bone-remodeling properties of porous silicon nanoparticles (pSiNPs) and calcium silicate coated pSiNPs (pCaSiNPs). (A, B) Scanning electron microscope images of pSiNPs (A) and pCaSiNPs (B). Images on the right indicate magnified views of the white boxes indicated in the left images. Scale bars indicate 100 nm (left) and 50 nm (right). (C) In vitro degradation kinetics of pSiNPs and pCaSiNPs under physiological conditions. The degradation kinetics were observed by measuring the relative count rate in pH 7.4 PBS at 37 °C using dynamic light scattering (DLS). The relative count rate by percent is defined as (%) = (count rate at a specific time point)/ (count rate at 0 h) × 100. (D) In vitro degradation kinetics of the calcium silicate coating on pCaSiNPs under physiological and inflammatory conditions. The degradation kinetics were observed by measuring the concentration of soluble calcium ions released from pCaSiNPs in pH 7.4 and pH 6 PBS buffers maintained at 37 °C, using inductively coupled plasma optical emission spectrometry (ICP-OES). (E) Flow cytometry analysis of immune cells treated with pSiNPs and pCaSiNPs. Bone marrow-derived dendritic cells (BMDCs) and bone marrow-derived macrophages (BMDMs) were treated with NPs for 24 h, and changes in expression level of costimulatory molecules (CD86 and CD40) were quantified by flow cytometry. Monophosphoryl lipid A (MPLA) was used as a positive control. (F) Counts of multinucleated osteoclasts per well at day 5 after pSiNP and pCaSiNP treatments. (G, H) Alkaline phosphatase (ALP) activity (G) and calcium deposition (H) analysis of osteoblasts after pSiNP and pCaSiNP treatments. ALP activity was analyzed from the cell medium at day 14. The quantity of calcium deposits was analyzed via Alizarin Red S staining at day 21. The dissolution byproducts Si(OH)4 and Ca2++Si(OH)4 in (F-H) were prepared at concentrations that correspond to the total amount of these species that could be produced upon complete dissolution of the nanoparticles used in the pSiNP and pCaSiNP experiments, respectively. Data in (C-H) represent mean \pm sd of at least three experimental replicates and are representative of at least two independent experiments. Sidak's multiple comparisons test was used for (D). One-way ANOVA followed by Tukey's post t test was used for (E-H) (*p < 0.05, **p < 0.01, ***p < 0.001, **** p < 0.0001; n.s., not significant).

(ICP-OES) measurements of the supernatants showed that pCaSiNPs released calcium ions more rapidly at pH 6.0 than at pH 7.4 (Figure 1D). This behavior is attributed to the preferential dissolution of the calcium silicate coating at the acidic pH.³² These results suggest that the calcium silicate coating can protect the pCaSiNPs from rapid dissolution in

blood (pH 7.4) but can promote cargo release at inflammation sites through a pH-dependent dissolution process.

We next evaluated the potential immunogenicity of the pSiNP and pCaSiNP nanocarriers, to ensure they would not stimulate immune cells and promote disease progression. Because RA is an autoimmune disease, the risk of the

Table 1. Hydrodynamic Size, Polydispersity Index, ζ Potential, and MTX Loading Efficiency of pSiNPs and pCaSiNPs^a

	pSiNP	pCaSiNP	pCaSiNP- MTX
hydrodynamic size (nm)	245 ± 92	262 ± 62	251 ± 88
polydispersity index	0.18 ± 0.03	0.20 ± 0.07	0.21 ± 0.07
ζ potential (mV)	-23.1 ± 7.6	-13.0 ± 7.1	-16.3 ± 7.1
mass loading (wt %)			21.6 ± 3.1

^aThe hydrodynamic size, polydispersity index, and ζ potential (surface charge) of pSiNPs, pCaSiNPs, and pCaSiNPs-MTX were analyzed by dynamic light scattering measurements. The loading efficiency of MTX in pCaSiNPs-MTX was given in weight percentage. The experiments were performed at least three times.

nanoparticles promoting unexpected immune responses is a particularly important consideration. Indeed, immune system activation has been observed with silicon oxide based nanoparticles (pSiO₂NPs).^{36–40} We treated bone marrow-

derived dendritic cells (BMDCs) and macrophages (BMDMs) with pSiNPs, pCaSiNPs, or monophosphoryl lipid A (MPLA, a positive control) for 24 h. A flow cytometry analysis revealed that the MPLA-treated BMDCs and BMDMs became activated and overexpressed costimulatory molecules, such as CD86 and CD40. In contrast, pSiNP- and pCaSiNP-treated cells exhibited no significant changes (Figure 1E). In addition, pSiNP and pCaSiNP treatments did not affect the expression of MHCII molecules in BMDCs and the secretion level of proinflammatory cytokines, such as tumor necrosis factor α (TNF- α) and interleukin (IL)-1 β , in BMDMs (Figure S3). The data indicate that the pCaSiNP nanocarriers can deliver the therapeutics to inflamed joints without initiating a negative immune response.

Bone-Remodeling Properties of pCaSiNPs. Since OSA has inhibitory effects on bone erosion and exerts anabolic functions on bone mineralization, ^{26,28} we first investigated if pSiNPs and pCaSiNPs and their dissolution/degradation products inhibit osteoclastogenesis that leads to RA. Raw 264.7 cells were differentiated into osteoclasts in RANKL-

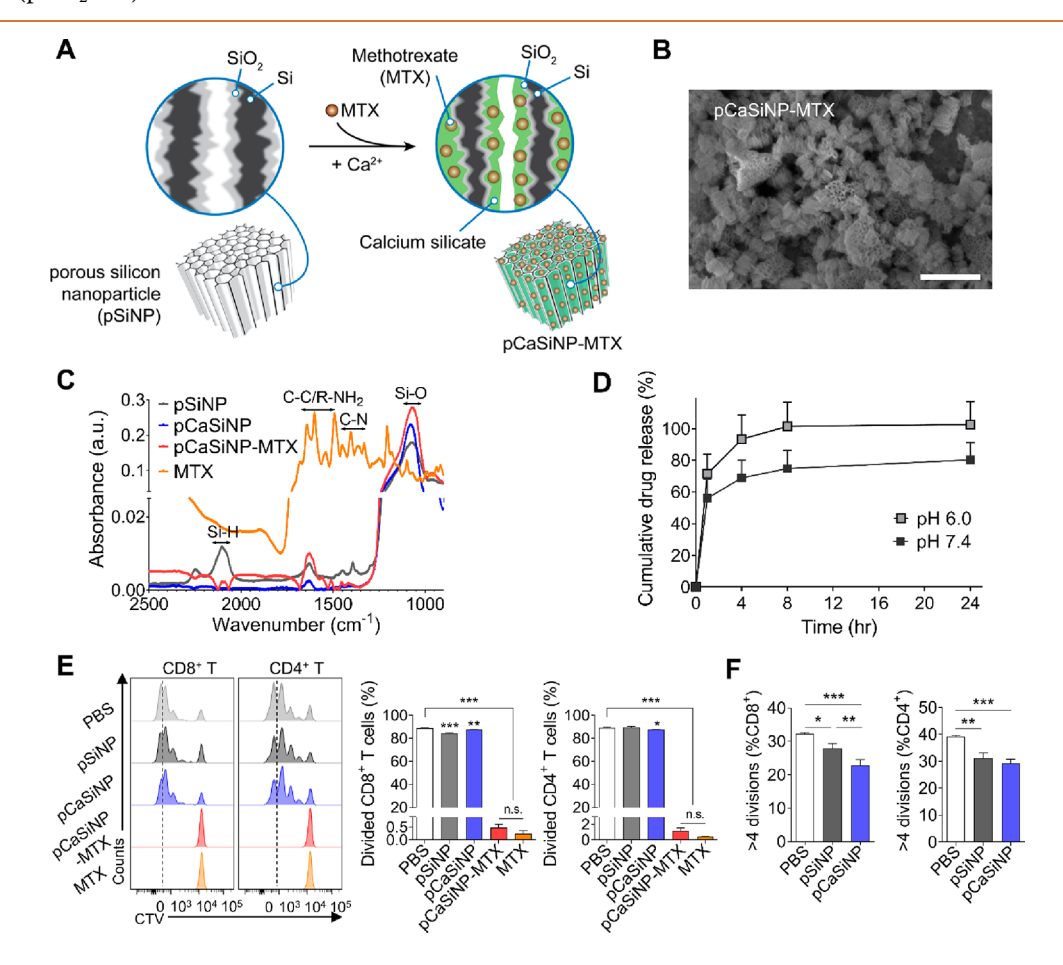


Figure 2. Physicochemical and immunomodulatory properties of methotrexate-loaded pCaSiNPs (pCaSiNPs-MTX). (A) Schematic representation showing *in situ* trapping of MTX in the calcium silicate layer for pCaSiNPs-MTX. (B) Scanning electron microscope image of pCaSiNPs-MTX. The scale bar indicates 500 nm. (C) Fourier transform infrared spectra of pSiNPs, pCaSiNPs, pCaSiNPs-MTX, and MTX. Modes assigned to C–C aromatic ring and R–NH₂ vibrations at 1675–1500 cm⁻¹ and C–N stretching at 1500–1400 cm⁻¹ indicate the absorption peaks of MTX. Si–H stretching was found at 2250 cm⁻¹ and Si–O stretching at 1080 cm⁻¹. (D) Drug release kinetics of pCaSiNPs-MTX in pH 7.4 PBS and pH 6.0 PBS at 37 °C. (E, F) Flow cytometry analysis of CellTrace Violet-labeled T cells treated with pSiNPs, pCaSiNPs-MTX, or MTX during coincubation with Dynabeads (α CD3/ α CD28 bead) at a 1/1 (cell to bead) ratio for 72 h. Proliferation of CD8⁺/CD4⁺ T cells (E) and percentage of CD8⁺/CD4⁺ T cells divided more than four times in (E) (F) were analyzed by flow cytometry. Data in (D–F) represent mean \pm sd of at least three experimental replicates and are representative of at least two independent experiments. One-way ANOVA followed by Tukey's post t test was used for (E) and (F) (*p < 0.05, **p < 0.01, ***p < 0.001; n.s., not significant).

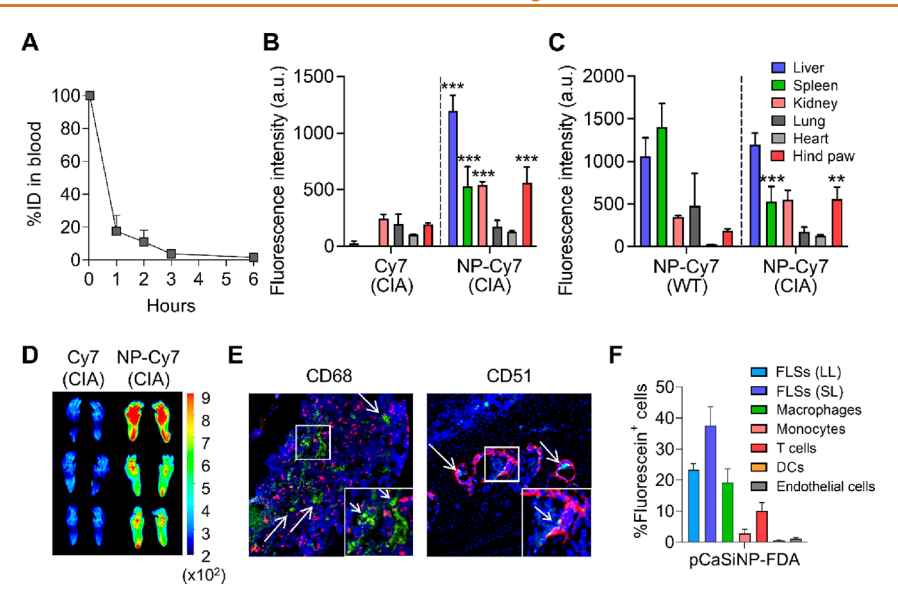


Figure 3. Passive accumulation and cellular distribution of pCaSiNPs in the inflamed paws of CIA mice. (A) Pharmacokinetics of ICG-loaded pCaSiNPs (pCaSiNPs-ICG). Blood samples were collected from the retro-orbital space at different time points after injection. (B) Biodistribution of Cy7 and Cy7-loaded pCaSiNPs (NP-Cy7) 6 h after injection in CIA mice. (C) Biodistribution of pCaSiNPs-Cy7 6 h after injection in wild-type (WT) and CIA mice. (D) Representative images of the inflamed hind paws 24 h after injection of Cy7 and NP-Cy7 in CIA mice. (E) Representative confocal fluorescence images of joint tissue sections 12 h after injection of fluorescein-conjugated pCaSiNPs (F-pCaSiNPs) in CIA mice. Synovial macrophages and osteoclasts were stained with CD68 (red, left) and CD51 (red, right), respectively. Green and blue signals indicate F-pCaSiNPs and nuclei (DAPI), respectively. The inset images (bottom right) represent magnified views of the white boxes. Arrows indicate colocalizations of F-pCaSiNPs and CD68 $^+$ cells or CD51 $^+$ cells. (F) Flow cytometry analysis of synovial cells 24 h after injection of fluorescein diacetate loaded pCaSiNPs (pCaSiNPs-FDA) in CIA mice. FLS and DC indicate fibroblast-like synoviocyte (LL, lining layer, PDPN $^+$ CD90.2 $^+$; SL, sublining layer, PDPN $^+$ CD90.2 $^+$) and dendritic cell, respectively. Data represent mean \pm sd. Two-way ANOVA followed by Tukey's multiple comparisons test was used for (B) and (C) (**p < 0.01, ***p < 0.001).

supplemented culture media. During the differentiation, we treated the cells with pSiNPs, pCaSiNPs, mesoporous silica nanoparticles (pSiO₂NPs), or the water-soluble dissolution products of the nanoparticles every 3 days. The water-soluble dissolution products of the nanoparticles were prepared by incubating each nanoparticle in phosphate-buffered saline (PBS) solution (pH 7.4) at 37 °C for 24 h, based on the results of a degradation kinetics study (Figure 1C). The pSiO₂NPs came from a commercial source (Sigma); this 200 nm silicon-based nanoparticle was composed of SiO₂ but contained no elemental Si. The pSiO₂NPs were chosen due to their chemical similarity to pSiNPs, though they tend to display slower dissolution kinetics under aqueous conditions. 41,42 None of these groups exhibited significant cytotoxicity toward Raw 264.7 cells at the tested dose (10 μ g/mL) and incubation period (48 h) (Figure S4A). Counting the number of osteoclasts (nuclei ≥ 3) per well on day 5 revealed that the pSiNP, pCaSiNP, and soluble byproduct treatments generated significantly fewer osteoclasts than PBS, whereas pSiO₂NPs did not hinder osteoclast formation (Figure 1F and Figure S5). We next studied whether pSiNPs, pCaSiNPs, and their dissolution byproducts enhance bone mineralization. MC3T3-E1 cells were treated with pSiNPs, pCaSiNPs or their dissolution byproducts in the differentiation media every 3 days. We analyzed the cellular alkaline phosphatase (ALP) activity and calcium deposition to assess bone mineralization. None of the groups demonstrated significant cytotoxicity against MC3T3-E1 cells at the tested dose and incubation period (Figure S4B). An ALP activity analysis revealed no functional changes among the groups (Figure 1G). However, treatment with pCaSiNPs and their dissolution byproducts, including both OSA and calcium ions,

significantly increased calcium mineralization independently of ALP activity in differentiated MC3T3-E1 cells (Figure 1H and Figure S6). Similar effects of extracellular calcium and OSA on osteogenic cellular differentiation have been observed in previous studies. Interestingly, the dissolution byproducts of pSiNPs also enhanced calcium mineralization, implying that the cells become sensitive to calcium deposition in a calcium ion containing culture medium via silicic acid induced autophagy. Collectively, these findings demonstrated that pCaSiNPs and their dissolution products boost bone remodeling in inflamed joints.

Immunomodulatory Properties of MTX-Loaded pCa-SiNPs. Next, we prepared MTX-loaded pCaSiNPs (pCa-SiNPs-MTX) by trapping MTX molecules into the calcium silicate layer in situ (Figure 2A,B). The average hydrodynamic size and surface charge measured by DLS were 251 ± 88 nm and -16.3 ± 7.1 mV, respectively (Table 1). The mass loading of MTX in the pCaSiNPs was $21.6 \pm 3.1\%$ (w/w), indicating that negatively charged MTX molecules (p K_a values of 4.8 and 5.5) exhibit strong association with the inorganic nanomaterial during the calcium silicate layer formation, presumably due to electrostatic interactions with the positively charged calcium ions.31 Furthermore, Fourier transform infrared (FTIR) spectra displayed bands characteristic of MTX (C-C/R-NH₂ vibration, 1675–1500 cm⁻¹; C-N stretching, 1500– 1400 cm⁻¹)⁴⁷ from the drug-loaded pCaSiNP-MTX construct but not from empty pCaSiNPs, verifying that MTX was indeed loaded into the pCaSiNPs (Figure 2C).

Since calcium silicate was found to preferentially dissolve under acidic pH conditions, we next assessed the kinetics of MTX release from pCaSiNPs in both blood- and inflammation-mimicking environments. For this purpose, we incubated

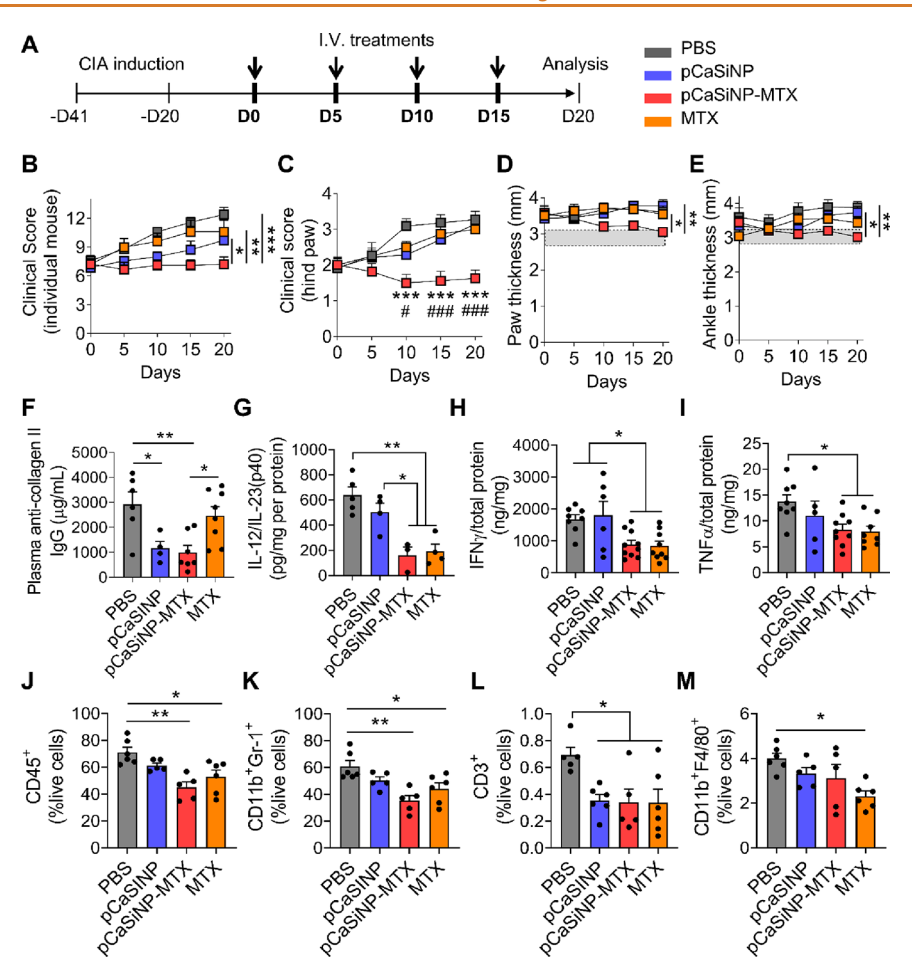


Figure 4. Antirheumatic efficacy of pCaSiNPs-MTX in CIA mice. (A) Schematic of the treatment plan. CIA mice were prepared by immunizing DBA/1J mice with collagen II emulsified in CFA (-D41) and collagen II emulsified in IFA (-D20). Mice were intravenously injected with PBS, pCaSiNPs, pCaSiNPs-MTX, or MTX (NP, 50 μ g; MTX, 0.54 mg/kg body weight) every 5 days until day 15. (B) Clinical score changes in individual mice during treatments. (C) Clinical score changes in hind paws. (D, E) Thickness of the paw (D) and ankle (E) in (C). Gray regions indicate the thickness range in wild-type mice (paw, 2.8–3.1 mm; ankle, 2.9–3.2 mm). (f) Anticollagen II IgG level in the plasma of treated mice. (G–I) Proinflammatory cytokine levels in the synovium of hind paws of treated mice: IL-12/23 (p40) (G), IFN γ (H), and TNF α (I). (J–M) Frequency of synovial immune cells in the hind paws of treated mice: total immune cells (CD45⁺) (J), Gr-1+myeloid cells (CD11b+Gr-1+) (K), T cells (CD3+) (L), and macrophages (CD11b+F4/80+) (M). Data represent mean \pm sem of at least four experimental replicates and are representative of at least two independent experiments. Two-way ANOVA followed by Tukey's multiple comparisons test was used for (B–E) (*p < 0.05, **p < 0.01, ***p < 0.001, ***p < 0.001).

pCaSiNPs-MTX in pH 7.4 (blood-mimicking) and pH 6.0 (inflammation-mimicking) solutions containing 10% fetal bovine serum (FBS) at 37 °C and measured the amount of MTX released over time. As expected, pCaSiNPs released MTX more rapidly in the pH 6.0 solution than in the pH 7.4 solution (Figure 2D). This supports the hypothesis that pCaSiNPs can preferentially release MTX in the acidic synovial fluid associated with RA.

One of the representative therapeutic functions of MTX in RA is the sensitizing of effector T cells to apoptosis. Thus, we next explored whether the calcium silicate trapping chemistry led to a loss of function of MTX by examining the suppressive function of MTX released from the nanoparticles on T cells. We labeled T cells isolated from splenocytes of wild-type mice with CellTrace Violet. Subsequently, we coincubated the cells with Dynabeads (which induce T cell activation and expansion) in the presence of pSiNPs, pCaSiNPs, pCaSiNPs-MTX, or free MTX for 72 h. Thereafter, we analyzed the CellTrace Violet signals of proliferating T cells by flow

cytometry. We observed that the MTX-loaded pCaSiNPs did not lose therapeutic function, as both free MTX and pCaSiNP-MTX inhibited the expansion of CD8⁺ and CD4⁺ T cells (Figure 2E). Additionally, significant immunomodulatory effects of pSiNPs and pCaSiNPs were observed in T cells that had divided more than four times (Figure 2F), indicating that the pCaSiNP dissolution byproducts augment the suppressive function of MTX on T cells. Therefore, we conclude that MTX loaded in pCaSiNPs suppresses the function of effector T cells in inflamed joints to an extent that is similar to, or greater than, that of free MTX.

Passive Targeting of pCaSiNPs in the Inflamed Synovium. Nanoparticle formulations passively accumulate in joints affected by RA by taking advantage of the leaky vasculature in an inflammation site. Thus, we next investigated the *in vivo* pharmacokinetics and biodistribution of pCaSiNPs in a mouse model of collagen-induced arthritis (CIA). We performed near-infrared (NIR) fluorescence imaging by loading pCaSiNPs with indocyanine green (ICG)

or Cy7 (pCaSiNPs-ICG or pCaSiNPs-Cy7, respectively) by following the protocol used for MTX loading. The CIA mouse model was generated by intradermally injecting an emulsion of type II collagen and complete Freund's adjuvant into the base of the mouse tail, followed by injecting an emulsion of type II collagen and incomplete Freund's adjuvant (IFA) after 3 weeks. The clinical score of RA was blindly assessed according to a scoring criteria. 50 Once the score of each hind paw reached 2 or 3, indicating swelling of the entire paw, we intravenously injected either pCaSiNPs-ICG or pCaSiNPs-Cy7 into the RA-induced mice. We first performed an in vivo pharmacokinetics study by analyzing blood samples taken at different time points by NIR fluorescence imaging. Quantification of blood fluorescence revealed that the injected pCaSiNPs-ICG circulated in the blood for 6 h (Figure 3A). We then conducted a biodistribution study, wherein we excised major organs, including the liver, spleen, kidneys, lungs, and hind paws 6 or 24 h postinjection and analyzed them with a NIR fluorescence imaging system. As expected, a considerable amount of the pCaSiNPs-Cy7 accumulated in the inflamed paws; indeed, the inflamed paws showed significantly higher pCaSiNP-Cy7 signals compared to injections of free Cy7 (Figure 3B). Similar to that observed with other nanoparticle formulations, 51,52 substantial quantities of pCaSiNPs-Cy7 were cleared from the blood by the organs of the mononuclear phagocyte system, such as the liver and the spleen. Additionally, we detected Cy7 fluorescence in the kidneys, implying that Cy7 molecules were released from the pCaSiNPs during blood circulation. Importantly, the inflamed paws showed significantly higher accumulation of pCaSiNPs-Cy7 than the healthy paws (Figure 3C). Furthermore, we observed prolonged accumulation of pCaSiNPs in the inflamed paws excised 24 h postinjection (Figure 3D). Collectively, these results demonstrated that systemically administered pCaSiNPs passively accumulate and remain in the inflamed joints.

Next, we investigated how pCaSiNPs deliver their intrinsic components and their loaded therapeutics to the diseased cells in the inflamed synovium. To examine the tissue distribution of pCaSiNPs, we chemically conjugated a fluorescein-NHS ester to amine-terminated pCaSiNPs (F-pCaSiNPs). Subsequently, we intravenously injected F-pCaSiNPs into the RAinduced mice and prepared hind paw tissue sections 12 h postinjection. Tissues were stained for CD68 and CD51 to identify inflammatory synovial macrophages⁵³ and osteoclasts,54 respectively. Immunofluorescence staining of the ankle tissue sections revealed that F-pCaSiNPs were distributed throughout the inflamed synovial tissue. Moreover, they colocalized to an extent with macrophages in the inflamed tissue and osteoclasts in the bone (Figure 3E). However, we detected a considerable number of F-pCaSiNPs in the acellular regions of the inflamed synovium, implying that pCaSiNPs release the loaded therapeutics at the inflammation sites via the pH-dependent calcium silicate dissolution process that was identified in the in vitro experiments.

Next, we determined which type of synovial cells the therapeutic agents targeted. For this set of experiments, we trapped fluorescein diacetate (FDA) in the calcium silicate layer of pCaSiNPs (pCaSiNPs-FDA); FDA is a cell-permeable esterase substrate that is hydrolyzed to fluorescein by intracellular esterases. The pCaSiNPs-FDA were intravenously injected into the RA-induced mice, and cells isolated from the hind paws 24 h postinjection were analyzed by flow cytometry.

We primarily observed fluorescein signals in FLSs, synovial macrophages, and T cells (Figure 3F). These results suggest that the pCaSiNPs accumulated in the inflamed joints can release their biodegradation products (OSA and calcium ions) and loaded therapeutics (e.g., MTX) to the localized T cells and FLSs. Small portions of the pCaSiNPs were observed to be directly taken up by phagocyte-like cells, such as synovial macrophages and osteoclasts.

Antirheumatic Properties of pCaSiNPs-MTX in CIA Mice. Having confirmed the synergistic potential of pCaSiNPs as drug carriers and antiresorptive agents, we next examined the antirheumatic properties of pCaSiNPs-MTX in the CIA mouse model (Figure 4A). Once the disease model had progressed such that all four paws of each mouse became inflamed (total RA score of 6-11), the mice were injected intravenously with PBS, pCaSiNPs (equivalent to the dose of pCaSiNPs in pCaSiNPs-MTX), pCaSiNPs-MTX, or free MTX (equivalent to the dose of MTX in pCaSiNPs-MTX) every 5 days until day 15. Mice treated with pCaSiNPs-MTX exhibited no disease progression, whereas those subjected to the other treatments gradually progressed to develop arthritis (Figure 4B). When only the hind paws with scores of 1-3 were examined, we observed that, while pCaSiNP-MTX treatment significantly reduced the arthritis score until day 20, the other treatments increased this score over the same period (Figure 4C). Moreover, the pCaSiNP-MTX treatment significantly reduced the paw and ankle thicknesses that indicate the extent of inflammation (Figure 4D,E), supporting the clinical score results. Furthermore, pCaSiNP-MTX treatment reversed the arthritis progression even in mice whose entire paws were inflamed and swollen (with a score of 3; Figure S7B). Notably, multiple doses of pCaSiNPs-MTX did not induce significant toxicities in the liver or kidneys, where the most common adverse effects of MTX are observed^{6,55} (Figure S8). This confirmed the biosafety of pCaSiNPs-MTX.

We next assessed the anticollagen II IgG levels, which is indicative of systemic arthritis progression, in blood collected from the treated mice at day 20. As expected, pCaSiNP-MTX treatment significantly lowered the anticollagen II IgG levels (Figure 4F). Interestingly, mice treated with pCaSiNPs also displayed significantly lowered anticollagen II IgG levels compared with untreated mice. Thus, we speculate that the dissolution byproducts of pCaSiNPs may have a therapeutic potential to manage RA without DMARDs. The antiarthritic effect of pCaSiNPs was also reflected in the clinical scores (Figure 4B and Figure S7A). Subsequently, we examined the immunological profiles of the synovium of the treated mice. Similar to the MTX treatment, the pCaSiNP-MTX treatment significantly reduced the levels of proinflammatory cytokines, including IL-12/23 (p40), interferon-gamma (IFN γ), and TNF α , in the synovium (Figure 4G–I). A flow cytometry analysis of synovial cell frequencies revealed that this treatment significantly reduced the total number of immune cells (CD45⁺), Gr-1⁺ myeloid cells (CD11b⁺Gr-1⁺), and T cells (CD3⁺) in the inflamed synovium; however, it did not reduce the levels of macrophages (CD11b+F4/80+; Figure 4J-M). These immunotherapeutic effects of pCaSiNPs-MTX were similar to those of the free MTX controls. Taken together, these results demonstrated that the pCaSiNPs efficiently deliver MTX to inflamed joints without compromising the function of MTX. Furthermore, they provide a therapeutic function on their own that improves the overall antirheumatic effects.

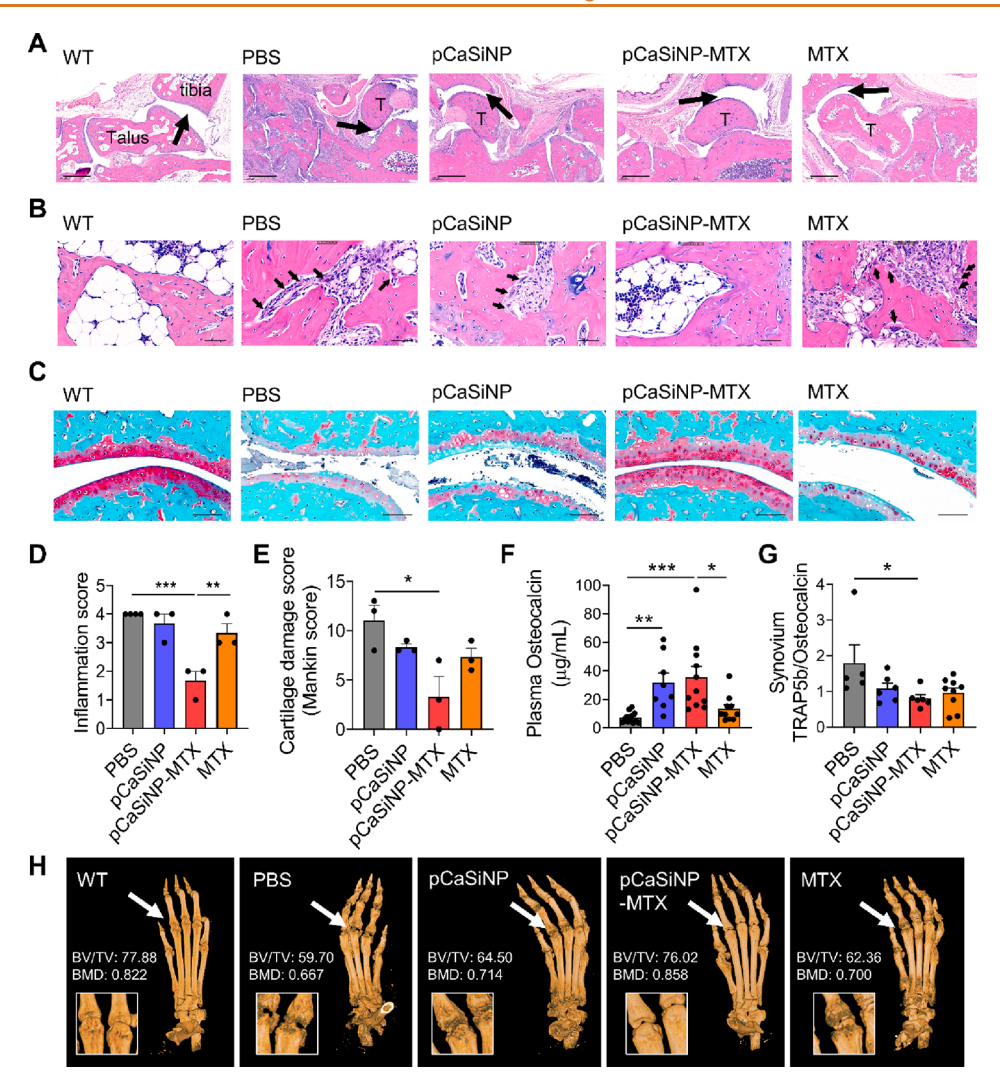


Figure 5. Anti-bone-erosion effects of pCaSiNPs-MTX in CIA mice. The treatment plan was the same as in Figure 4A. At day 20, the hind paws were excised for histological analysis and microCT imaging, and osteocalcin and tartrate-resistant acid phosphatase 5b (TRAP5b) levels in the plasma and the synovial fluids were analyzed by ELISA. (A, B) Representative hematoxylin and eosin stained images of inflamed joint tissues after treatments showing the gap between talus and tibia (indicated with arrows) (A) and the multinucleated osteoclasts in bone marrow (indicated with arrows) (B). T indicates talus. Scale bars indicate $500 \,\mu\text{m}$ in (A) and $50 \,\mu\text{m}$ in (B). (C) Representative Safranin-O stained images of inflamed joint tissues after treatments. The cells stained in red indicate the chondrocytes. The scale bar indicates $100 \,\mu\text{m}$. (D, E) Histological scores of inflammation (D) and cartilage damage (E) according to the criteria. (F) Osteocalcin level in the plasma of treated mice. (G) Ratio of TRAP5b to osteocalcin in the synovial fluids of treated mice. (H) MicroCT images of the hind paws and joints of treated mice. The insets (left bottom) represent magnified images of toe joints indicated with white arrows. WT, BV/TV, and BMD indicate wild-type mice, bone volume/tissue volume ratio, and bone mineral density, respectively. Data in (D-G) represent mean \pm sem of at least three experimental replicates and are representative of at least two independent experiments. One-way ANOVA followed by Tukey's post t test was used for (D-G) (*p < 0.05, **p < 0.01, ***p < 0.001).

Antiresorptive Properties of pCaSiNPs-MTX in CIA

Mice. We next evaluated the anti-bone resorption properties of pCaSiNPs-MTX that could be synergistically combined with the immunomodulatory effects of MTX to effectively treat advanced RA. In this regard, we harvested the hind paws of the treated mice and prepared tissue sections for histological analysis. Hematoxylin and eosin (H&E) staining of the ankle sections demonstrated that the pCaSiNP-MTX treatment dramatically reduced immune cell infiltration and multinucleated osteoclast formation compared to the other treatments (Figure 5A,B). Furthermore, a histological analysis revealed that the pCaSiNP-MTX treatment had the lowest inflammation score among all the treatments (Figure 5D). Interestingly, Safranin-O staining of the cartilage sections showed that cartilage damage was reduced upon the pCaSiNP-

MTX treatment; this was evident by the clear joint space and red staining of chondrocytes (Figure 5C). An analysis of the histopathological images using the Mankin scoring criteria showed that the pCaSiNP-MTX treatment resulted in the lowest level of cartilage damage among all the treatments (Figure 5E).

We next assessed the levels of bone biomarkers in the blood plasma and synovial fluids collected from the treated mice. The level of plasma osteocalcin (bone generation marker) was significantly increased in both the pCaSiNP and pCaSiNP-MTX treatments, reflecting the effects of the biodegradation products (Figure 5F). Furthermore, the pCaSiNP-MTX treatment significantly reduced the ratio of tartrate-resistant acid phosphatase 5b (TRAP5b, bone resorption marker) to osteocalcin in the inflamed synovium compared to the PBS

treatment, indicating their local effects on the balance of bone remodeling (Figure 5G). The microCT images of hind paws and joints also revealed that the pCaSiNP-MTX treatment more effectively preserved the joints from bone erosion compared to other treatments (Figure 5H). The bone volume/tissue volume ratio (BV/TV) and bone mineral density (BMD) values derived from the microCT analysis are given in Figure 5H. The nanoparticle-treated group showed increases in both BV/TV and BMD values relative to the controls. In particular, these values in the pCaSiNP-MTXtreated group increased to levels comparable to those in the wild type (healthy) animals. The trends in the BV/TV and BMD data from the representative images in Figure 5H are consistent with the quantitative measures of systemic and local bone biomarkers given in Figure 5F,G. These findings demonstrated that the pCaSiNP-MTX treatment minimized bone erosion in RA by synergistically combining the immunomodulatory effects of MTX with the bone-remodeling properties of pCaSiNPs. The equivalent dose of MTX monotherapy failed to preserve the joints from bone erosion, despite its ability to successfully reduce inflammation.

DISCUSSION

Rheumatoid arthritis is a chronic inflammatory disorder that is characterized by synovial inflammation and bone degradation. Inflammatory processes in RA pathogenesis alter the balance of the osteoblast—osteoclast axis, leading to elevated bone resorption. Although MTX is the most strongly recommended drug for RA treatment, according to the ACR guidelines, repeated doses intensify RA-induced bone resorption via osteoclast formation and chondrocyte apoptosis. The Clinically, denosumab has been combined with MTX to increase bone mineral density and reduce bone turnover in RA patients. In this study, we used pCaSiNPs-MTX to achieve such synergistic therapeutic effects in RA.

OSA (orthosilicic acid) is the bioavailable form of silicon found in humans and animals. Recently, several studies have indicated that it can be beneficial to bone regeneration because it inhibits osteoclastogenesis and stimulates bone mineralization. 26-28 In addition, one study reported that silicon-based biomaterials (e.g., bioactive glass) degrade into OSA and inhibit osteoclast formation and bone resorption in vitro. 56 Among many of the silicon-based biomaterials available, we chose pSiNPs for RA treatment because they can rapidly dissolve into OSA under physiological conditions and they can efficiently encapsulate various drugs in their mesoporous structure. 57-59 Furthermore, their surfaces can be readily coated with a biodegradable calcium silicate layer; 31,60 calcium is known to be a necessary component for bone mineralization. We found that the byproducts of pCaSiNP dissolution, i.e., OSA and calcium ions, effectively inhibited osteoclastic differentiation and stimulated bone mineralization in osteoblasts (Figure 1F-H).

Nanoparticle formulations of MTX have been extensively investigated for RA. This is because they can efficiently localize MTX to the inflamed joints by taking advantage of the leaky vasculature in these tissues. Indeed, various MTX-loaded nanoparticles based on liposomes, 61,62 proteins, 63,64 and organic 65,66 and inorganic components 67 have been developed to improve therapeutic outcomes relative to free MTX. The data of Figure 3B,C show that the pCaSiNP construct also effectively accumulated in the regions of the inflamed joints. The calcium silicate condenser chemistry used in the present

work provided a high mass loading of the MTX payload in the pCaSiNPs of $21.6 \pm 3.1\%$ (w/w). For comparison, the best liposomal formulations of MTX display only 1% mass loading. In addition to their ability to carry a substantially larger quantity of the therapeutic MTX payload, we hypothesized that the pCaSiNPs would be able to synergize with MTX for RA treatment. Two synergistic effects were considered: first, we expected the acidic environment of the inflamed synovium to trigger dissolution of the nanoparticles, releasing the MTX payload locally at the disease site to minimize potential liver and kidney toxicity; second, we expected the calcium(II) and silicate byproducts of nanoparticle dissolution to show beneficial effects due to their known bone-remodeling properties.

Nanoparticle formulations are often taken up by phagocytes, such as macrophages and dendritic cells.⁶⁹ However, confocal fluorescence microscopy of joint tissue sections indicated that a substantial portion of the pCaSiNP cargo delivered to the inflamed synovium was localized to the acellular regions (Figure 3E), and a flow cytometry analysis of the infiltrated cells indicated that the cargo was localized to the T cells as well as the synovial phagocytes (FLSs and macrophages) (Figure 3F). Consistent with the pH-triggered release process identified in vitro (Figure 2D), pCaSiNPs-MTX delivered substantial immunomodulatory effects to inflamed tissues in vivo, though the data do not indicate if the MTX cargo was released from the pCaSiNPs in the intracellular regions after cellular uptake of the pCaSiNPs or if the cargo was released from the pCaSiNPs in the extracellular regions before cellular uptake and then transferred into the cells. We attribute the observed suppression of inflammatory events in the RA joints to the high level of accumulation of the nanoparticles in the inflamed tissues, leading to their localized, pH-triggered release of MTX in the vicinity of immune cells, particularly T cells and

The CIA model is the most commonly used model of RA because bone and cartilage damage and immune cell infiltration into the joint space are similar to what is observed in human RA.70 In most of the published studies on CIA models, treatments have been administered from the early stage of RA (clinical score of 0-1 in each paw), when the swelling and erythema of the ankle and paw joints would start to appear. 63,71,72 Here, we treated CIA mice at the early stage (clinical score of 1 or 2 in each paw) and at the established stage where inflammation and bone erosion actively occurred (clinical score of 3 in each paw; Figure 4A–E and Figure S7). Notably, MTX monotherapy was not effective in halting disease progression regardless of when the treatment was initiated. However, pCaSiNPs-MTX exhibited significant antirheumatic effects at both the early and the established stages, indicating that the combined effects of MTX and pCaSiNP byproducts effectively managed both joint inflammation and bone erosion in RA. The injected dose of pCaSiNPs-MTX used in the present study corresponded to 10.8 μ g of MTX (corresponding to 0.54 mg/kg). This dosing was selected because it is below the therapeutic dose window for free MTX; thus, the antiarthritis effect observed with pCaSiNPs-MTX could not be achieved by MTX alone. Moreover, a recent study has demonstrated that CIA symptoms at the established stage are relieved with MTXloaded nanoparticles;⁶⁵ however, the dose of MTX (5 mg/kg) in that study was ~10 times higher than the 0.54 mg/kg dose used in the present study.

Interestingly, treatment with empty (i.e., not loaded with MTX) pCaSiNPs was also found to slow disease progression, although the extent of modulation was weaker than that of the pCaSiNP-MTX treatment (p < 0.05 between pCaSiNP and PBS at day 15 as shown in Figure 4B; p < 0.05 between pCaSiNP and PBS at day 10 as shown in Figure S7A). We attribute the efficacy of the empty pCaSiNPs to their immunomodulatory effect on T cell proliferation (Figures 2E,F and 4L) and to their beneficial effects on bone remodeling (Figures 1F,H and 5F). It has been reported that OSA inhibits TNFα-induced activation of NF-κB in osteoblasts by upregulating the expression of microRNA-146a. 73 MicroRNA-146a is a negative feedback regulator of NF-κB activity and suppresses T cell activation, acute responses, and chronic autoimmune responses. 74,75 Based on these molecular mechanisms, we propose that OSA, as a byproduct of pCaSiNP dissolution, plays a critical role in regulating T cell activation and proliferation. Since proinflammatory cytokines have been reported to activate NF-κB in various RA-related cells, including innate immune cells, T cells, B cells, and fibroblasts, ⁷⁶ it is possible that a pCaSiNP monotherapy might exert antirheumatic effects by inhibiting NF-κB pathways in these cells. However, this proposed mechanism needs to be studied in more detail.

CONCLUSIONS

In summary, the therapeutic potential of a porous silicon-based nanomedicine for the effective management of both inflammation and bone erosion in RA was demonstrated in an animal model. The use of the term "nanomedicine" here refers to the fact that, while the nanoparticle carries and releases a drug similar to the majority of conventional nanodelivery systems, the nanoparticle itself is composed of constituents that also show a beneficial effect in treating the disease. The intravenously injected pCaSiNP-MTX construct accumulated efficiently in the inflamed joints and dissolved in the acidic environment, releasing as byproducts the antiresorptive substances OSA and calcium ion. These byproducts are endogenous substances in mammalian tissues, and so they lower the risk of immunogenic response. Furthermore, the dissolution byproducts, delivered through in vivo dissolution of the pCaSiNP vehicle, managed bone erosion in the animal model of RA. When the construct also contained an antirheumatic drug payload (MTX), significant reduction of inflammation in the joints was observed. Together, the drug and biodegradation products localized in the inflamed joints exhibited synergistic therapeutic effects in RA by simultaneously managing inflammation and bone resorption. The high capacity of the nanoparticles for loading of MTX suggests that pCaSiNPs might also be effective carriers for other antiarthritic agents such as glucocorticoids and antibody-based biological DMARDs, which underscores the translational potential of this porous silicon-based nanomedicine for RA treatment.

MATERIALS AND METHODS

Preparation of Porous Silicon Nanoparticles (pSiNPs) and Calcium Silicate Coated pSiNPs (pCaSiNPs). Highly boron doped p^{++2} -type single-crystal silicon wafers ($\sim 1~m\Omega$ cm resistivity, polished on the (100) face) were obtained from Virginia Semiconductor, Inc. or Siltronix, Inc. Porous silicon samples were prepared by electrochemical etching of silicon wafers in an electrolyte consisting of 3/1 (by volume) aqueous 48% hydrofluoric acid (HF)/ethanol (EtOH). (*Caution*! HF is highly toxic and proper care should be used to avoid

contact with skin or lungs.) A silicon working electrode with an exposed area of 9.6 cm² was contacted on the back side with aluminum foil and mounted in a Teflon cell and then subjected to galvanostatic anodization in a two-electrode configuration using a platinum-coil counter electrode. Prior to the main preparation step of the pSi layers, the silicon wafer was cleaned in a two-step process. First, the surface was anodized in the electrolyte (HF/EtOH 3/1 by volume) to generate a thin layer of pSi, commonly called a "sacrificial layer" of porous silicon (pSi). The resulting pSi layer was then dissolved in an aqueous potassium hydroxide solution (2 M KOH) and rinsed thoroughly using deionized water and ethanol. The resulting clean silicon surface was then anodized by application of a square waveform, alternating between a lower current density of 50 mA/cm² applied for 1.82 s followed by a higher current density of 400 mA/cm² applied for 0.363 s. This etching waveform was repeated for 300 cycles in order to generate a "perforated" pSi film consisting of 300 layers approximately 200 nm thick, each separated by highporosity layers (the "perforations"). The above etching protocol was selected to maximize the mass loading of the MTX therapeutic in the resulting nanoparticles; when the lower current density value was 30 mA/cm² (as opposed to 50 mA/cm²), the mean pore size was smaller (~10 vs ~14 nm) and the mass loading of MTX was lower. When current densities >70 mA/cm² were used for the lower current density phase of the etching waveform, the nanoparticle size distribution was uneven. The perforated pSi film was lifted off by etching at a constant current density of 3.1 mA/cm² for 300 s in an electrolyte composed of 1/12 (by volume) aqueous 48% HF/ethanol solution, followed by ultrasonication in deionized water for 24 h to produce nanoparticles. The larger (>1 μ m) fragments remaining were removed by sedimentation for 1 h, and then the supernatant was centrifuged at 15000 rpm for 23 min, producing a pellet of nanoparticles. The supernatant was removed and discarded, and the nanoparticles were resuspended and centrifuged at 15000 rpm for 23 min three more times, first in deionized water, then in 70% ethanol, and finally in 100% ethanol. The prepared NPs were stored in 100% ethanol for further studies and resuspended prior to use. The silicon and calcium concentrations in the NPs were measured by inductively coupled plasma optical emission spectrometry (ICP-OES). The surface charge and hydrodynamic size of NPs were measured using a dynamic light scattering instrument (Malvern Panalytical, UK).

Preparation of Cargo-Loaded and Fluorophore-Conjugated pCaSiNPs. pSiNPs were maintained in deionized water at 5 mg (Si)/ mL at 4 °C for at least 5 days to preoxidize them before cargo loading. To prepare methotrexate-loaded pCaSiNPs (pCaSiNPs-MTX), methotrexate hydrate (Sigma) was dissolved in dimethyl sulfoxide (DMSO) at 10 mg/mL. A 100 μ L portion of the preoxidized pSiNP dispersion was gently mixed with 40 μ L of methotrexate solution, and 1 mL of an aqueous 4 M calcium chloride (CaCl₂, Sigma) solution was added to form the calcium silicate layer. The sample was ultrasonicated for 3 min and incubated overnight with gentle rocking. Unloaded MTX was removed by washing the nanoparticles with distilled water (DW) at least three times by centrifugation at 15000 rpm for 23 min. The surface charge and hydrodynamic size of pCaSiNPs-MTX were measured by dynamic light scattering (Malvern Panalytical, UK). To calculate the loading capacity of MTX, pCaSiNPs-MTX were dissolved in 2 M KOH and the absorbance was measured at 300 nm by a UV/vis spectrophotometer (Molecular Devices). The amount of MTX was calculated from a standard curve created with free MTX.

To prepare fluorophore-loaded pCaSiNPs, indocyanine green (ICG, Tokyo Chemical Industry), Cy7-NHS-ester (Cy7, Lumiprobe), and fluorescein diacetate (FDA, Sigma) were dissolved in DMSO at 1, 1, and 10 mg/mL, respectively. A 100 μ L portion of preoxidized pSiNP solution was mixed with 40 μ L of fluorophore solution, and 1 mL of 4 M CaCl₂ solution was added to incubate for 12 h. Unloaded fluorophores were removed by several washes with deionized water by centrifugation. To prepare fluorescein-conjugated pCaSiNP (FpCaSiNP), 100 μ L of the preoxidized pSiNP suspension was incubated with 1 mL of aqueous 4 M CaCl₂ solution overnight. After several washes with deionized water by centrifugation, 500 μ g

(Si) of pCaSiNPs was resuspended in 500 μ L of ethanol and reacted with 12.5 μ L of 3-aminopropyldimethylethoxysilane (APDMES) for 2 h. After several washes with ethanol by centrifugation, the amineterminated pCaSiNPs were reacted with 375 μ g of fluorescein-NHS ester (Thermo Scientific, in 10 μ L of DMSO) in 250 μ L of 0.1 M Tris buffer (pH 8.4) for 4 h. Unloaded fluorescein molecules were removed by several washes with deionized water by centrifugation.

Cell Isolation and Culture. Raw 264.7 cells were cultured in DMEM supplemented with 10% fetal bovine serum (FBS) (Hyclone, UT, USA) and 1% penicillin/streptomycin (Hyclone, UT, USA) before starting differentiation. For osteoclast differentiation, Raw 264.7 cells were cultured in α MEM supplemented with 10% FBS, 1% penicillin/streptomycin, and RANKL (Sigma) (20 ng/mL). MC3T3-E1 preosteoblast cells (subclone 4) were cultured in ascorbic acid free αMEM (Gibco, A10490) supplemented with 10% FBS and 1% penicillin/streptomycin. For osteoblast differentiation, MC3T3-E1 cells were cultured in α MEM supplemented with 10% FBS, 1% penicillin/streptomycin, ascorbic acid (150 µg/mL) (Sigma), 10 mM β -glycerophosphate (Sigma), and 10 nM dexamethasone (Sigma). Bone marrow cells were isolated from the femur and tibia of 6-7week-old C57BL/6N mice. For bone marrow-derived dendritic cells (BMDCs), the cells were cultured in RPMI supplemented with 10% FBS, 1% penicillin/streptomycin, and granulocyte-macrophage colony-stimulating factor (GM-CSF) (20 ng/mL). For bone marrow-derived macrophages (BMDMs), the cells were cultured in DMEM supplemented with 10% FBS, 1% penicillin/streptomycin, and macrophage colony-stimulating factor (M-CSF) (20 ng/mL). For splenic T cells, splenocytes were isolated from the spleen of 6-7week-old C57BL/6N mice. Spleens were gently minced and pressed through a 70 μ m cell strainer, while continuously adding culture media. Red blood cells were lysed by incubating the cells in ACK lysis buffer for 5 min on ice, followed by centrifugation (2000 rpm, 10 min). Cells were resuspended with magnetic-activated cell sorting (MACS) buffer containing 0.5% BSA and 2 mM EDTA. T lymphocytes were collected with a Pan T cell isolation kit using MACS (Miltenyi Bio). Collected T cells were washed by centrifugation and cultured in RPMI supplemented with 10% FBS, 1% penicillin/streptomycin, and 50 μ M 2-mercaptoethanol (Sigma). All cells were incubated in a 5% CO₂ incubator at 37 °C.

Degradation Kinetics. A 50 μ g portion (Si) of NPs was incubated in 1 mL of pH 7.4 PBS or pH 6.0 PBS (adjusted by addition of 1 M HCl) at 37 °C. To determine the presence of NPs in the solution, the count rate of the sample was measured at each time point (0, 0.5, 1, 2, 3, 4, and 8 h) by dynamic light scattering (DLS) measurements (Malvern). The relative count rate by percent is defined as (%) = (count rate at specific time point)/(count rate at 0 h) × 100. To determine the pH-dependent degradation of the calcium silicate coating, pCaSiNP samples were incubated in either pH 6 or pH 7.4 solutions for 0.5, 1, and 4 h and the dissolved calcium in the incubated sample was separated from residual NPs by centrifugation. The calcium ion concentration in the supernatant at each time point was quantified by ICP-OES measurements.

Immunogenicity. BMDMs were treated with pSiNP, pSiNP byproduct, pCaSiNP, or pCaSiNP byproduct at 10 μ g (Si)/mL for 24 h. Monophosphoryl Lipid A (MPLA) at 1 μ g/mL was used as a positive control for activation of the cells. The cells were detached in Accutase cell dissociation reagent (Thermo Scientific), labeled with fluorophore-conjugated antibodies, and analyzed by flow cytometry. The culture supernatants were collected after centrifugation, and the levels of TNF α and IL-1 β were measured by ELISA (Thermo Scientific).

In Vitro Bone-Remodeling Effects. The byproducts of NPs were prepared by dissolving 50 μ g (Si) of NPs in 1 mL of PBS at 37 °C for 24 h. To study the effects of NPs and their byproducts on osteoclastogenesis, the osteoclasts differentiated from Raw 264.7 cells were treated with 10 μ g (Si)/mL of pSiNPs, the dissolution byproduct of pSiNPs, pCaSiNPs, the dissolution byproduct of pCaSiNPs, or commercially available mesoporous silica nanoparticles with an average size of 200 nm (pSiO₂NPs, Sigma-Aldrich) every 3 days until day 5. At day 5, a TRACP & ALP assay (TAKARA) was

performed according to the manufacturer's protocol. Multinucleated osteoclasts (nuclei ≥3) in a well were counted as differentiated osteoclasts and imaged with an optical microscope (Nikon). To study the effects of NPs and their byproducts on bone mineralization, MC3T3-E1 cells were treated with 10 μ g/mL of pSiNPs, the dissolution byproduct of pSiNPs, pCaSiNPs, or the dissolution byproduct of pCaSiNPs in the differentiation media every 3 days until day 21. At day 14, an alkaline phosphatase assay (Abcam) was performed according to the manufacturer's protocol. At day 21, an Alizarin Red S staining assay (Sigma) was performed for visualization of calcium deposits produced by differentiated osteoblasts. For the cell viability assays, 1×10^4 of Raw 264.7 cells or 5×10^3 of MC3T3-E1 cells were seeded and cultured in a 96-well plate for 24 h. The cells were then treated with 10 µg (Si)/mL of pSiNPs, pCaSiNPs, their dissolution byproducts, or pSiO₂NPs for 48 h. To determine the viable cells, Cell Counting Kit-8 assays were performed according to the manufacturer's protocol.

Drug Release Kinetics. A 50 μ g (Si) portion of pCaSiNPs-MTX was incubated in 0.5 mL of pH 7.4 PBS or pH 6.0 PBS (adjusted by addition of 1 M HCl) with 10% fetal bovine serum (FBS) at 37 °C. To determine the release kinetics of MTX from pCaSiNPs-MTX, the supernatants were collected at each time point (0, 1, 4, 8, and 24 h) by centrifugation (15000 rpm, 23 min). Absorbance of the released MTX in the supernatants was measured by a UV/vis spectrophotometer. The amount of unloaded MTX was calculated from the MTX absorbance at 300 nm utilizing a standard curve created with free MTX.

Ex Vivo Proliferation Assay of CD4⁺ and CD8⁺ T Cells. Splenic T cells were labeled with CellTrace Violet (CTV) dye (Thermo Scientific) according to the manufacturer's protocol. A 2 \times 10⁵ amount of CTV-labeled T cells was seeded in a 96-well plate and incubated with Dynabeads (mouse T-Activator CD3/CD28) in the presence of pSiNPs, pCaSiNPs, pCaSiNPs-MTX, or free MTX for 72 h. The treated concentrations of NPs and MTX were 50 μ g (Si)/mL and 1.25 μ g/mL, respectively. After incubation, the cells were collected, labeled with fluorophore-conjugated antibodies, and analyzed by flow cytometry.

Mouse Model of Collagen-Induced Arthritis. All animal procedures were approved by the Animal Care and Use committees at KAIST. DBA/1J mice and C57BL/6N mice were purchased from Orient Bio and Koatech, respectively (South Korea). For induction of collagen-induced arthritis (CIA) in mice, 2 mg/mL of type II collagen solution (Chondrex) and 4 mg/mL of complete Freund's adjuvant (CFA, Chondrex) were emulsified at a ratio of 1/1 and injected intradermally in the base of the tail of each 12-week-old male DBA/1J mouse. After 3 weeks, a booster shot with an emulsion of type II collagen and incomplete Freund's adjuvant (IFA) (Chondrex) was intradermally injected. The clinical score of RA was observed weekly until it became the appropriate score for each experiment. The assessment of clinical score was performed blindly in accordance with the scoring criteria (0 = normal, 1 = one swelling toe, 2 = two or more swelling toes or mild inflammation of entire paw, 3 = severe inflammation of entire paw, 4 = ankylosed toe).50

Blood Circulation. A 50 μ g (Si) portion of pCaSiNPs-ICG was intravenously injected into the tail veins of CIA-induced mice with paw scores of 2 and 3. At each time point after injection (0.03, 1, 2, 3, and 6 h), the mouse plasma was collected by retro-orbital bleeding, followed by centrifugation (3000 rpm, 15 min) at 4 °C. The ICG fluorescence in the plasma was detected via an LI-COR imaging system (LI-COR Biosciences, NE).

Biodistribution. A 50 μ g (Si) portion of pCaSiNPs-Cy7 and an amount of free Cy7 with the same fluorescence intensity as pCaSiNPs-Cy7 were intravenously injected into the tail veins of CIA-induced mice with paw scores of 2 and 3 or wild-type mice. To allow for complete hydrolysis of NHS esters prior to injection, Cy7-NHS esters were incubated in PBS for 1 day. At 6 and 24 h postinjection, major organs including liver, spleen, kidney, heart, lung, and hind paws were excised after perfusing the mice with 0.9% saline. The major organs were then imaged with an LI-COR imaging system. To examine the cellular distribution in the inflamed synovium, 50 μ g

(Si) of pCaSiNPs-FDA was intravenously injected into the tail veins of CIA-induced mice with paw scores of 2 and 3. At 24 h postinjection, the hind paws were excised after perfusing the mice with 0.9% saline, and the cells in the hind paws were isolated for flow cytometry analysis. To examine the tissue distribution in the inflamed synovium, 50 μ g (Si) of F-pCaSiNPs was intravenously injected into the tail veins of CIA-induced mice with paw scores of 2 and 3. At 12 h postinjection, the hind paws were excised after perfusing the mice with 0.9% saline, fixed with 10% neutral buffered formalin (NBF) for 2 days, and decalcified with 1 M EDTA solution for 2-3 weeks. The tissues were sectioned and stained with PE antimouse CD68 antibody (Biolegend) or PE antimouse CD51 antibody (Biolegend), followed by 4',6-diamidino-2-phenylindole (DAPI) staining. The stained tissues were imaged with a confocal microscope (Nikon). The tissue surrounding the tibia was imaged for CD68-stained sections, while the bone marrow was imaged for CD51-stained sections.

Flow Cytometry Analysis. The skin and muscle tissue of the excised hind legs were removed by gently touching so as not to break the bone tissue. The hind leg tissues were incubated in 1 mL of icecold PBS supplemented with Complete Protease Inhibitor Cocktail (Sigma), followed by vigorous vortexing for 15 min at 4 °C. The tissues were then incubated with RPMI supplemented with 1 mg/mL of collagenase IV solution (Gibco) and 50 U/mL of DNase I (Thermo scientific) at 37 °C for 1 h, followed by incubation with RPMI supplemented with 1 mg/mL of collagenase/Dispase solution (Sigma) and 50 U/mL of DNase I at 37 °C for 30 min. All supernatants were centrifuged at 350g for 5 min to collect the synovial cells. The cells were stained with fluorophore-conjugated antibodies at 4 °C for 30 min. The antibodies used are given in Table S1. The cells were gated using the following strategies: FLS (lining layer), CD45-PDPN+CD90.2-; FLS (sublining layer), CD45⁻PDPN⁺CD90.2⁺; macrophage, CD45⁺CD11b⁺F4/80⁺; monocyte, CD45⁺CD11b⁺Ly6c⁺; Gr-1⁺myeloid cell, CD45⁺CD11b⁺Gr-1⁺; T cell, CD45⁺CD3; dendritic cells, CD45⁺ CD11c⁺MHCII⁺; endothelial cells, CD45⁻CD31⁺.

In Vivo Therapy of CIA-Induced Mice. CIA-induced mice with clinical scores of 6-11 (or paw scores of 1-3) were intravenously injected with PBS, pCaSiNPs, pCaSiNPs-MTX, or MTX every 5 days until day 15 of the study. a 50 μg (Si) portion of NPs and 10.8 μg of MTX were injected per mouse. The assessment of the clinical score was performed blindly, and the thicknesses of each paw and ankle were measured with a caliper before each injection. At day 20, the plasma samples were collected for assessment of organ toxicity and the hind paws were excised for an assessment of synovial cell populations. The plasma samples were stored at -80 °C. The plasma levels of aspartate aminotransferase (AST), alanine aminotransferase (ALT), and blood urea nitrogen (BUN) were measured using an AU480 chemistry analyzer (Beckman). Synovial fluids were collected by incubating the hind paw tissues in 1 mL of ice-cold PBS supplemented with Complete Protease Inhibitor Cocktail (Sigma), followed by vigorous vortexing for 15 min at 4 °C. The supernatant was stored at -80 °C for ELISA. The levels of antibovine collagen II IgG (Chondrex), IL-12/IL-23(p40) (Thermo Scientific), IFNγ (Thermo Scientific), TNF α (Thermo Scientific), osteocalcin (Novus Biologicals), and TRAP5b (Mybiosource) in the plasma and synovial fluid were measured via ELISA. The synovial cells were prepared with the aforementioned procedure and analyzed by flow cytometry.

Histological Analysis. The excised hind paws were fixed with 10% NBF for 2 days and decalcified with 1 M EDTA solution for 2–3 weeks. The tissues were embedded in paraffin, and 5 μm thick sections were imaged using a micro-CT scanner (SkyScan 1173, Bruker). The bone-erosion-related parameters, including bone volume/tissue volume ratio (BV/TV) and bone mineral density (BMD), were measured by image analysis programs (Genoss, South Korea). The sections were also stained with hematoxylin and eosin (H&E) and Safranin-O. H&E staining and Safranin-O staining were performed using standard protocols. The histological scoring of inflammation was performed in accordance with the following scoring criteria (0, normal; 1, mild thickening of lining layer or mild

infiltration of cells in the sublining layer; 2, mild thickening of lining layer and mild infiltration of cells in the sublining layer; 3, severe infiltration of cells and presence of cells in synovial space; 4, severe infiltration of cells in synovial space).⁷⁷ The histological scoring of cartilage destruction was performed in accordance with the Mankin scoring criteria.⁷⁸

Statistical Analysis. The level of significance in all statistical analyses was set at p < 0.05. Data were analyzed using the unpaired Student's t test for two groups or one-way analysis of variance (ANOVA) or two-way ANOVA for three or more groups followed by Tukey's multiple comparisons test using Prism 8.4 (GraphPad Software).

ASSOCIATED CONTENT

Supporting Information

The Supporting Information is available free of charge at https://pubs.acs.org/doi/10.1021/acsnano.2c04491.

Additional *in vitro/in vivo* experimental data related to particle characteristics, immunomodulatory/bone remodeling properties, toxicity, and therapeutic efficacy (PDF)

AUTHOR INFORMATION

Corresponding Authors

Ji-Ho Park – Department of Bio and Brain Engineering and KAIST Institute for Health Science and Technology, Korea Advanced Institute of Science and Technology (KAIST), Daejeon 34141, Republic of Korea; ⊚ orcid.org/0000-0002-0721-0428; Email: jihopark@kaist.ac.kr

Dokyoung Kim – Department of Biomedical Science, Graduate School, Kyung Hee University, Seoul 02447, Republic of Korea; Email: dkim@khu.ac.kr

Authors

Moonkyoung Jeong – Department of Bio and Brain Engineering and KAIST Institute for Health Science and Technology, Korea Advanced Institute of Science and Technology (KAIST), Daejeon 34141, Republic of Korea

Yuna Jung – Department of Biomedical Science, Graduate School, Kyung Hee University, Seoul 02447, Republic of Korea

Junyong Yoon – Department of Bio and Brain Engineering and KAIST Institute for Health Science and Technology, Korea Advanced Institute of Science and Technology (KAIST), Daejeon 34141, Republic of Korea

Jinyoung Kang — Department of Nanoengineering, University of California, San Diego, La Jolla, California 92093, United States; Present Address: McGovern Institute for Brain Research, Massachusetts Institute of Technology, Cambridge, MA 02139, USA

Seo Hyeon Lee – Department of Biomedical Science, Graduate School, Kyung Hee University, Seoul 02447, Republic of Korea

Woojin Back – Department of Bio and Brain Engineering and KAIST Institute for Health Science and Technology, Korea Advanced Institute of Science and Technology (KAIST), Daejeon 34141, Republic of Korea

Hyoyeon Kim – Department of Bio and Brain Engineering and KAIST Institute for Health Science and Technology, Korea Advanced Institute of Science and Technology (KAIST), Daejeon 34141, Republic of Korea

Michael J. Sailor – Department of Nanoengineering and Department of Chemistry and Biochemistry, University of California, San Diego, La Jolla, California 92093, United States; orcid.org/0000-0002-4809-9826

Complete contact information is available at: https://pubs.acs.org/10.1021/acsnano.2c04491

Author Contributions

M.J. and J.-H.P. conceived and designed the research. M.J., Y.J., J.K., S.H.L., and D.K. prepared the porous silicon materials. M.J., J.Y., W.B., and H.K. carried out the experiments. M.J., Y.J., J.Y., J.K., M.J.S., D.K., and J.-H.P. analyzed the data. M.J., M.J.S., and J.-H.P. wrote the manuscript.

Notes

The authors declare the following competing financial interest(s): M.J.S. is a scientific founder (SF), member of the Board of Directors (BOD), Advisory Board (AB), Scientific Advisory Board (SAB), acts as a paid consultant (PC) or has an equity interest (EI) in the following: Aivocode, Inc (AB, EI); Bejing ITEC Technologies (SAB, PC); Cend Therapeutics (SF, BOD, EI); Illumina (EI), Matrix Technologies (EI); NanoVision Bio (SAB, EI); Pacific Integrated Energy (AB; EI); Quanterix (EI), Spinnaker Biosciences, Inc. (SF, BOD, EI); TruTag Technologies (SAB, EI); and Well-Healthcare Technologies (SAB, PC). M.I.S. is also a Guest Professor at Zhejiang University, China. Although one or more of the grants that supported this research has been identified for conflict of interest management based on the overall scope of the project and its potential benefit to the companies listed, the research findings included in this publication may not necessarily relate to their interests. The terms of these arrangements have been reviewed and approved by the University of California, San Diego in accordance with its conflict of interest policies. The other authors declare no competing financial interests.

ACKNOWLEDGMENTS

This work was supported by the Basic Science Research Program through the National Research Foundation (NRF-2017R1E1A1A01074847, NRF-2018R1A6A1A03025124, and NRF-2021R1A2C2094074) funded by the Ministry of Science and ICT, Republic of Korea. This research was partially supported by the NSF through the UC San Diego Materials Research Science and Engineering Center (UCSD MRSEC, DMR-2011924).

REFERENCES

- (1) Lin, Y. J.; Anzaghe, M.; Schulke, S. Update on the Pathomechanism, Diagnosis, and Treatment Options for Rheumatoid Arthritis. *Cells* **2020**, *9* (4), 880.
- (2) Briot, K.; Roux, C. Glucocorticoid-induced osteoporosis. *RMD Open* **2015**, *1* (1), No. e000014.
- (3) Fraenkel, L.; Bathon, J. M.; England, B. R.; St Clair, E. W.; Arayssi, T.; Carandang, K.; Deane, K. D.; Genovese, M.; Huston, K. K.; Kerr, G.; Kremer, J.; Nakamura, M. C.; Russell, L. A.; Singh, J. A.; Smith, B. J.; Sparks, J. A.; Venkatachalam, S.; Weinblatt, M. E.; Al-Gibbawi, M.; Baker, J. F.; Barbour, K. E.; Barton, J. L.; Cappelli, L.; Chamseddine, F.; George, M.; Johnson, S. R.; Kahale, L.; Karam, B. S.; Khamis, A. M.; Navarro-Millan, I.; Mirza, R.; Schwab, P.; Singh, N.; Turgunbaev, M.; Turner, A. S.; Yaacoub, S.; Akl, E. A. 2021 American College of Rheumatology Guideline for the Treatment of Rheumatoid Arthritis. *Arthritis Care Res.* (Hoboken) 2021, 73 (7), 924–939
- (4) Cronstein, B. N.; Aune, T. M. Methotrexate and its mechanisms of action in inflammatory arthritis. *Nat. Rev. Rheumatol* **2020**, *16* (3), 145–154.

- (5) Buchen, S.; Ngampolo, D.; Melton, R. G.; Hasan, C.; Zoubek, A.; Henze, G.; Bode, U.; Fleischhack, G. Carboxypeptidase G2 rescue in patients with methotrexate intoxication and renal failure. *Br. J. Cancer* **2005**, 92 (3), 480–7.
- (6) Moghadam, A. R.; Tutunchi, S.; Namvaran-Abbas-Abad, A.; Yazdi, M.; Bonyadi, F.; Mohajeri, D.; Mazani, M.; Marzban, H.; Los, M. J.; Ghavami, S. Pre-administration of turmeric prevents methotrexate-induced liver toxicity and oxidative stress. *BMC Complement Altern Med.* **2015**, *15*, 246.
- (7) Fan, C. M.; Foster, B. K.; Hui, S. K.; Xian, C. J. Prevention of bone growth defects, increased bone resorption and marrow adiposity with folinic acid in rats receiving long-term methotrexate. *PLoS One* **2012**, *7* (10), No. e46915.
- (8) King, T. J.; Shandala, T.; Lee, A. M.; Foster, B. K.; Chen, K. M.; Howe, P. R.; Xian, C. J. Potential Effects of Phytoestrogen Genistein in Modulating Acute Methotrexate Chemotherapy-Induced Osteoclastogenesis and Bone Damage in Rats. *Int. J. Mol. Sci.* **2015**, *16* (8), 18293–311.
- (9) Smolen, J. S.; Aletaha, D.; Barton, A.; Burmester, G. R.; Emery, P.; Firestein, G. S.; Kavanaugh, A.; McInnes, I. B.; Solomon, D. H.; Strand, V.; Yamamoto, K. Rheumatoid arthritis. *Nat. Rev. Dis Primers* **2018**, *4*, 18001.
- (10) Solomon, D. H.; Kay, J.; Duryea, J.; Lu, B.; Bolster, M. B.; Yood, R. A.; Han, R.; Ball, S.; Coleman, C.; Lo, E.; Wohlfahrt, A.; Sury, M.; Yin, M.; Yu, Z.; Zak, A.; Gravallese, E. M. Effects of Teriparatide on Joint Erosions in Rheumatoid Arthritis: A Randomized Controlled Trial. *Arthritis Rheumatol* **2017**, *69* (9), 1741–1750.
- (11) Iwamoto, N.; Sato, S.; Sumiyoshi, R.; Chiba, K.; Miyamoto, N.; Arinaga, K.; Kobayashi, M.; Yamamoto, H.; Osaki, M.; Kawakami, A. Comparative study of the inhibitory effect on bone erosion progression with denosumab treatment and conventional treatment in rheumatoid arthritis patients: study protocol for an open-label randomized controlled trial by HR-pQCT. *Trials* **2019**, *20* (1), 494.
- (12) Subbiah, V.; Madsen, V. S.; Raymond, A. K.; Benjamin, R. S.; Ludwig, J. A. Of mice and men: divergent risks of teriparatide-induced osteosarcoma. *Osteoporos Int.* **2010**, *21* (6), 1041–5.
- (13) Spanakis, E. K.; Sellmeyer, D. E. Nonuremic calciphylaxis precipitated by teriparatide [rhPTH(1-34)] therapy in the setting of chronic warfarin and glucocorticoid treatment. *Osteoporos Int.* **2014**, 25 (4), 1411–4.
- (14) Cohen, S. B.; Dore, R. K.; Lane, N. E.; Ory, P. A.; Peterfy, C. G.; Sharp, J. T.; van der Heijde, D.; Zhou, L.; Tsuji, W.; Newmark, R. Denosumab Rheumatoid Arthritis Study, G., Denosumab treatment effects on structural damage, bone mineral density, and bone turnover in rheumatoid arthritis: a twelve-month, multicenter, randomized, double-blind, placebo-controlled, phase II clinical trial. *Arthritis Rheum* 2008, 58 (5), 1299–309.
- (15) Zhang, N.; Zhang, Z. K.; Yu, Y.; Zhuo, Z.; Zhang, G.; Zhang, B. T. Pros and Cons of Denosumab Treatment for Osteoporosis and Implication for RANKL Aptamer Therapy. *Front Cell Dev Biol.* **2020**, *8*, 325.
- (16) Takeuchi, T.; Tanaka, Y.; Soen, S.; Yamanaka, H.; Yoneda, T.; Tanaka, S.; Nitta, T.; Okubo, N.; Genant, H. K.; van der Heijde, D. Effects of the anti-RANKL antibody denosumab on joint structural damage in patients with rheumatoid arthritis treated with conventional synthetic disease-modifying antirheumatic drugs (DESIRABLE study): a randomised, double-blind, placebo-controlled phase 3 trial. *Ann. Rheum Dis* **2019**, *78* (7), 899–907.
- (17) Jeong, M.; Park, J. H. Nanomedicine for the Treatment of Rheumatoid Arthritis. *Mol. Pharmaceutics* **2021**, *18* (2), 539–549.
- (18) Shi, J.; Kantoff, P. W.; Wooster, R.; Farokhzad, O. C. Cancer nanomedicine: progress, challenges and opportunities. *Nat. Rev. Cancer* **2017**, *17* (1), 20–37.
- (19) Santos, H. A.; Makila, E.; Airaksinen, A. J.; Bimbo, L. M.; Hirvonen, J. Porous silicon nanoparticles for nanomedicine: preparation and biomedical applications. *Nanomedicine* (*Lond*) **2014**, 9 (4), 535–54.

- (20) Park, J. H.; Gu, L.; von Maltzahn, G.; Ruoslahti, E.; Bhatia, S. N.; Sailor, M. J. Biodegradable luminescent porous silicon nanoparticles for in vivo applications. *Nat. Mater.* **2009**, 8 (4), 331–6.
- (21) Granitzer, P.; Rumpf, K. Porous Silicon—A Versatile Host Material. *Materials* **2010**, 3 (2), 943–998.
- (22) Wang, C. F.; Makila, E. M.; Kaasalainen, M. H.; Hagstrom, M. V.; Salonen, J. J.; Hirvonen, J. T.; Santos, H. A. Dual-drug delivery by porous silicon nanoparticles for improved cellular uptake, sustained release, and combination therapy. *Acta Biomater* **2015**, *16*, 206–14.
- (23) Whitehead, M. A.; Fan, D.; Mukherjee, P.; Akkaraju, G. R.; Canham, L. T.; Coffer, J. L. High-porosity poly(epsilon-caprolactone)/mesoporous silicon scaffolds: Calcium phosphate deposition and biological response to bone precursor cells. *Tissue Eng. Part A* **2008**, *14* (1), 195–206.
- (24) Sun, W.; Puzas, J. E.; Sheu, T. J.; Liu, X.; Fauchet, P. M. Nanoto microscale porous silicon as a cell interface for bone-tissue engineering. *Adv. Mater.* **2007**, *19* (7), 921–924.
- (25) Canham, L., Porous silicon for medical use: from conception to clinical use. In *Porous Silicon for Biomedical Applications*; Woodhead Publishing: 2014; pp 3–20.
- (26) Costa-Rodrigues, J.; Reis, S.; Castro, A.; Fernandes, M. H. Bone Anabolic Effects of Soluble Si: In Vitro Studies with Human Mesenchymal Stem Cells and CD14+ Osteoclast Precursors. *Stem Cells Int.* **2016**, 2016, 1–12.
- (27) Chi, H.; Kong, M.; Jiao, G.; Wu, W.; Zhou, H.; Chen, L.; Qiao, Y.; Wang, H.; Ma, W.; Chen, Y. The role of orthosilicic acid-induced autophagy on promoting differentiation and mineralization of osteoblastic cells. *J. Biomater Appl.* **2019**, *34* (1), 94–103.
- (28) Ma, W.; Wang, F.; You, Y.; Wu, W.; Chi, H.; Jiao, G.; Zhang, L.; Zhou, H.; Wang, H.; Chen, Y. Ortho-silicic Acid Inhibits RANKL-Induced Osteoclastogenesis and Reverses Ovariectomy-Induced Bone Loss In Vivo. *Biol. Trace Elem Res.* **2021**, *199* (5), 1864–1876.
- (29) Canham, L. T. Bioactive Silicon Structure Fabrication Through Nanoetching Techniques. *Adv. Mater.* **1995**, *7* (12), 1033–1037.
- (30) Bronner, F. Extracellular and intracellular regulation of calcium homeostasis. *Sci. World J.* **2001**, *1*, 919–25.
- (31) Kang, J.; Joo, J.; Kwon, E. J.; Skalak, M.; Hussain, S.; She, Z.-G.; Ruoslahti, E.; Bhatia, S. N.; Sailor, M. J. Self-Sealing Porous Silicon-Calcium Silicate Core—Shell Nanoparticles for Targeted siRNA Delivery to the Injured Brain. *Adv. Mater.* **2016**, *28*, 7962–7969.
- (32) Medina-Gonzales, O.; Fox, R.; Bosshart, R. Solubility and availability to sugarcane (Saccharum spp.) of two silicate materials. *Fertilizer research* **1988**, *16* (1), 3–13.
- (33) Qin, Z.; Joo, J.; Gu, L.; Sailor, M. J. Size Control of Porous Silicon Nanoparticles by Electrochemical Perforation Etching. *Particle & Particle Systems Characterization* **2014**, *31* (2), 252–256.
- (34) Zhang, D. X.; Yoshikawa, C.; Welch, N. G.; Pasic, P.; Thissen, H.; Voelcker, N. H. Spatially Controlled Surface Modification of Porous Silicon for Sustained Drug Delivery Applications. *Sci. Rep* **2019**, 9 (1), 1367.
- (35) Goldie, I.; Nachemson, A. Synovial pH in rheumatoid knee joints. II. The effect of local corticosteroid treatment. *Acta Orthop Scand* **1970**, *41* (3), 354–62.
- (36) Wang, X.; Li, X.; Ito, A.; Watanabe, Y.; Sogo, Y.; Tsuji, N. M.; Ohno, T. Stimulation of In Vivo Antitumor Immunity with Hollow Mesoporous Silica Nanospheres. *Angew. Chem., Int. Ed. Engl.* **2016**, *55* (5), 1899–903.
- (37) Wang, X.; Li, X.; Yoshiyuki, K.; Watanabe, Y.; Sogo, Y.; Ohno, T.; Tsuji, N. M.; Ito, A. Comprehensive Mechanism Analysis of Mesoporous-Silica-Nanoparticle-Induced Cancer Immunotherapy. *Adv. Healthc. Mater.* **2016**, *5* (10), 1169–76.
- (38) Heidegger, S.; Gößl, D.; Schmidt, A.; Niedermayer, S.; Argyo, C.; Endres, S.; Bein, T.; Bourquin, C. Immune response to functionalized mesoporous silica nanoparticles for targeted drug delivery. *Nanoscale* **2016**, *8* (2), 938–948.
- (39) Kupferschmidt, N.; Qazi, K. R.; Kemi, C.; Vallhov, H.; Garcia-Bennett, A. E.; Gabrielsson, S.; Scheynius, A. Mesoporous silica particles potentiate antigen-specific T-cell responses. *Nanomedicine* **2014**, 9 (12), 1835–1846.

- (40) Mahony, D.; Cavallaro, A. S.; Stahr, F.; Mahony, T. J.; Qiao, S. Z.; Mitter, N. Mesoporous silica nanoparticles act as a self-adjuvant for ovalbumin model antigen in mice. *Small* **2013**, *9* (18), 3138–46.
- (41) Tang, F.; Li, L.; Chen, D. Mesoporous silica nanoparticles: synthesis, biocompatibility and drug delivery. *Adv. Mater.* **2012**, *24* (12), 1504–34.
- (42) Croissant, J. G.; Fatieiev, Y.; Khashab, N. M. Degradability and Clearance of Silicon, Organosilica, Silsesquioxane, Silica Mixed Oxide, and Mesoporous Silica Nanoparticles. *Adv. Mater.* **2017**, 29 (9), 1604634.
- (43) Cheng, S.; Wang, W.; Lin, Z.; Zhou, P.; Zhang, X.; Zhang, W.; Chen, Q.; Kou, D.; Ying, X.; Shen, Y.; Cheng, X.; Yu, Z.; Peng, L.; Lu, C. Effects of extracellular calcium on viability and osteogenic differentiation of bone marrow stromal cells in vitro. *Hum Cell* **2013**, 26 (3), 114–20.
- (44) Gonzalez-Vazquez, A.; Planell, J. A.; Engel, E. Extracellular calcium and CaSR drive osteoinduction in mesenchymal stromal cells. *Acta Biomater* **2014**, *10* (6), 2824–33.
- (45) Reffitt, D. M.; Ogston, N.; Jugdaohsingh, R.; Cheung, H. F.; Evans, B. A.; Thompson, R. P.; Powell, J. J.; Hampson, G. N. Orthosilicic acid stimulates collagen type 1 synthesis and osteoblastic differentiation in human osteoblast-like cells in vitro. *Bone* **2003**, *32* (2), 127–35.
- (46) Eapen, A.; Sundivakkam, P.; Song, Y.; Ravindran, S.; Ramachandran, A.; Tiruppathi, C.; George, A. Calcium-mediated stress kinase activation by DMP1 promotes osteoblast differentiation. *J. Biol. Chem.* **2010**, 285 (47), 36339–51.
- (47) Ayyappan, S.; Sundaraganesan, N.; Aroulmoji, V.; Murano, E.; Sebastian, S. Molecular structure, vibrational spectra and DFT molecular orbital calculations (TD-DFT and NMR) of the antiproliferative drug Methotrexate. *Spectrochim Acta A Mol. Biomol Spectrosc* **2010**, 77 (1), 264–75.
- (48) Torchilin, V. Tumor delivery of macromolecular drugs based on the EPR effect. Adv. Drug Deliv Rev. 2011, 63 (3), 131-5.
- (49) Paleolog, E. M. Angiogenesis in rheumatoid arthritis. *Arthritis Res.* **2002**, *4* (Suppl 3), S81–90.
- (50) Brand, D. D.; Latham, K. A.; Rosloniec, E. F. Collagen-induced arthritis. *Nat. Protoc* **2007**, *2* (5), 1269–75.
- (51) Poon, W.; Kingston, B. R.; Ouyang, B.; Ngo, W.; Chan, W. C. W. A framework for designing delivery systems. *Nat. Nanotechnol* **2020**, *15* (10), 819–829.
- (52) Li, S. D.; Huang, L. Pharmacokinetics and biodistribution of nanoparticles. *Mol. Pharmaceutics* **2008**, 5 (4), 496–504.
- (53) Tu, J.; Wang, X.; Gong, X.; Hong, W.; Han, D.; Fang, Y.; Guo, Y.; Wei, W. Synovial Macrophages in Rheumatoid Arthritis: The Past, Present, and Future. *Mediators Inflamm* **2020**, 2020, 1–8.
- (54) Zallone, A. Z.; Teti, A.; Gaboli, M.; Marchisio, P. C. Beta 3 subunit of vitronectin receptor is present in osteoclast adhesion structures and not in other monocyte-macrophage derived cells. *Connect Tissue Res.* **1989**, 20 (1–4), 143–149.
- (55) Harms, J.; Khawaja, A.; Taylor, M.; Han, X.; Mrug, M. Recovery of methotrexate-induced anuric acute kidney injury after glucarpidase therapy. *SAGE Open Med. Case Rep* **2017**, *S*, 2050313X17705050.
- (56) Mladenovic, Z.; Johansson, A.; Willman, B.; Shahabi, K.; Bjorn, E.; Ransjo, M. Soluble silica inhibits osteoclast formation and bone resorption in vitro. *Acta Biomater* **2014**, *10* (1), 406–18.
- (57) Kwon, E. J.; Skalak, M.; Bertucci, A.; Braun, G.; Ricci, F.; Ruoslahti, E.; Sailor, M. J.; Bhatia, S. N. Porous Silicon Nanoparticle Delivery of Tandem Peptide Anti-Infectives for the Treatment of Pseudomonas aeruginosa Lung Infections. *Adv. Mater.* **2017**, 29 (35), 1701527.
- (58) Bimbo, L. M.; Denisova, O. V.; Makila, E.; Kaasalainen, M.; De Brabander, J. K.; Hirvonen, J.; Salonen, J.; Kakkola, L.; Kainov, D.; Santos, H. A. Inhibition of influenza A virus infection in vitro by saliphenylhalamide-loaded porous silicon nanoparticles. *ACS Nano* **2013**, 7 (8), 6884–93.
- (59) Gu, L.; Ruff, L. E.; Qin, Z.; Corr, M.; Hedrick, S. M.; Sailor, M. J. Multivalent porous silicon nanoparticles enhance the immune

- activation potency of agonistic CD40 antibody. Adv. Mater. 2012, 24 (29), 3981-7.
- (60) Kim, B.; Pang, H.-B.; Kang, J.; Park, J.-H.; Ruoslahti, E.; Sailor, M. J. Immunogene therapy with fusogenic nanoparticles modulates macrophage response to Staphylococcus aureus. *Nat. Commun.* **2018**, *9*, 1969.
- (61) Alekseeva, A. A.; Moiseeva, E. V.; Onishchenko, N. R.; Boldyrev, I. A.; Singin, A. S.; Budko, A. P.; Shprakh, Z. S.; Molotkovsky, J. G.; Vodovozova, E. L. Liposomal formulation of a methotrexate lipophilic prodrug: assessment in tumor cells and mouse T-cell leukemic lymphoma. *Int. J. Nanomedicine* **2017**, *12*, 3735–3749.
- (62) Ali, M. F.; Salah, M.; Rafea, M.; Saleh, N. Liposomal methotrexate hydrogel for treatment of localized psoriasis: preparation, characterization and laser targeting. *Med. Sci. Monit* **2008**, *14* (12), PI66–P174.
- (63) Liu, L.; Hu, F.; Wang, H.; Wu, X.; Eltahan, A. S.; Stanford, S.; Bottini, N.; Xiao, H.; Bottini, M.; Guo, W.; Liang, X. J. Secreted Protein Acidic and Rich in Cysteine Mediated Biomimetic Delivery of Methotrexate by Albumin-Based Nanomedicines for Rheumatoid Arthritis Therapy. ACS Nano 2019, 13 (5), 5036–5048.
- (64) Lyu, J.; Wang, L.; Bai, X.; Du, X.; Wei, J.; Wang, J.; Lin, Y.; Chen, Z.; Liu, Z.; Wu, J.; Zhong, Z. Treatment of Rheumatoid Arthritis by Serum Albumin Nanoparticles Coated with Mannose to Target Neutrophils. ACS Appl. Mater. Interfaces 2021, 13 (1), 266–276
- (65) Zhong, S.; Liu, P.; Ding, J.; Zhou, W. Hyaluronic Acid-Coated MTX-PEI Nanoparticles for Targeted Rheumatoid Arthritis Therapy. *Crystals* **2021**, *11* (4), 321.
- (66) Ha, Y. J.; Lee, S. M.; Mun, C. H.; Kim, H. J.; Bae, Y.; Lim, J. H.; Park, K. H.; Lee, S. K.; Yoo, K. H.; Park, Y. B. Methotrexate-loaded multifunctional nanoparticles with near-infrared irradiation for the treatment of rheumatoid arthritis. *Arthritis Res. Ther* **2020**, 22 (1), 146.
- (67) Alvarez-Gonzalez, B.; Rozalen, M.; Fernandez-Perales, M.; Alvarez, M. A.; Sanchez-Polo, M. Methotrexate Gold Nanocarriers: Loading and Release Study: Its Activity in Colon and Lung Cancer Cells. *Molecules* **2020**, *25* (24), 6049.
- (68) Che, J.; Najer, A.; Blakney, A. K.; McKay, P. F.; Bellahcene, M.; Winter, C. W.; Sintou, A.; Tang, J.; Keane, T. J.; Schneider, M. D.; Shattock, R. J.; Sattler, S.; Stevens, M. M. Neutrophils Enable Local and Non-Invasive Liposome Delivery to Inflamed Skeletal Muscle and Ischemic Heart. *Adv. Mater.* **2020**, 32 (48), No. 2003598.
- (69) Hardy, C. L.; Lemasurier, J. S.; Mohamud, R.; Yao, J.; Xiang, S. D.; Rolland, J. M.; O'Hehir, R. E.; Plebanski, M. Differential uptake of nanoparticles and microparticles by pulmonary APC subsets induces discrete immunological imprints. *J. Immunol* **2013**, *191* (10), 5278–90.
- (70) Luan, J.; Hu, Z.; Cheng, J.; Zhang, R.; Yang, P.; Guo, H.; Nan, G.; Guo, N.; Gou, X. Applicability and implementation of the collagen-induced arthritis mouse model, including protocols (Review). *Exp Ther Med.* **2021**, *22* (3), 939.
- (71) Yan, F.; Zhong, Z.; Wang, Y.; Feng, Y.; Mei, Z.; Li, H.; Chen, X.; Cai, L.; Li, C. Exosome-based biomimetic nanoparticles targeted to inflamed joints for enhanced treatment of rheumatoid arthritis. *J. Nanobiotechnology* **2020**, *18* (1), 115.
- (72) Zhang, Q.; Dehaini, D.; Zhang, Y.; Zhou, J.; Chen, X.; Zhang, L.; Fang, R. H.; Gao, W.; Zhang, L. Neutrophil membrane-coated nanoparticles inhibit synovial inflammation and alleviate joint damage in inflammatory arthritis. *Nat. Nanotechnol* **2018**, *13* (12), 1182–1190.
- (73) Zhou, X.; Moussa, F. M.; Mankoci, S.; Ustriyana, P.; Zhang, N.; Abdelmagid, S.; Molenda, J.; Murphy, W. L.; Safadi, F. F.; Sahai, N. Orthosilicic acid, Si(OH)4, stimulates osteoblast differentiation in vitro by upregulating miR-146a to antagonize NF-kappaB activation. *Acta Biomater* **2016**, *39*, 192–202.
- (74) Boldin, M. P.; Taganov, K. D.; Rao, D. S.; Yang, L.; Zhao, J. L.; Kalwani, M.; Garcia-Flores, Y.; Luong, M.; Devrekanli, A.; Xu, J.; Sun, G.; Tay, J.; Linsley, P. S.; Baltimore, D. miR-146a is a significant brake

- on autoimmunity, myeloproliferation, and cancer in mice. *J. Exp Med.* **2011**, 208 (6), 1189–201.
- (75) Yang, L.; Boldin, M. P.; Yu, Y.; Liu, C. S.; Ea, C. K.; Ramakrishnan, P.; Taganov, K. D.; Zhao, J. L.; Baltimore, D. miR-146a controls the resolution of T cell responses in mice. *J. Exp Med.* **2012**, 209 (9), 1655–70.
- (76) Liu, T.; Zhang, L.; Joo, D.; Sun, S. C. NF-kappaB signaling in inflammation. Signal Transduct Target Ther 2017, 2, 17023.
- (77) Moon, J.; Kim, D.; Kim, E. K.; Lee, S. Y.; Na, H. S.; Kim, G. N.; Lee, A.; Jung, K.; Choi, J. W.; Park, S. H.; Roh, S.; Cho, M. L. Brown adipose tissue ameliorates autoimmune arthritis via inhibition of Th17 cells. *Sci. Rep* **2020**, *10* (1), 12374.
- (78) Mankin, H. J.; Dorfman, H.; Lippiello, L.; Zarins, A. Biochemical and metabolic abnormalities in articular cartilage from osteo-arthritic human hips. II. Correlation of morphology with biochemical and metabolic data. *J. Bone Joint Surg Am.* **1971**, *53* (3), 523–37.

□ Recommended by ACS

Porous Silicon Carrier Endowed with Photothermal and Therapeutic Effects for Synergistic Wound Disinfection

Wei Duan, Jianmin Wu, et al.

OCTOBER 24, 2022

ACS APPLIED MATERIALS & INTERFACES

READ 🗹

Tumor-Homing and Immune-Reprogramming Cellular Nanovesicles for Photoacoustic Imaging-Guided Phototriggered Precise Chemoimmunotherapy

Zhijin Fan, Liming Nie, et al.

SEPTEMBER 22, 2022

ACS NANO

READ 🗹

High-Efficiency Treatment for Osteoarthritis via Self-Assembled Dual-Functionalized Nanobiologics

Chenyu Wang, Jingjing Li, et al.

JULY 08, 2022

ACS BIOMATERIALS SCIENCE & ENGINEERING

READ 🗹

Caffeic Acid Modified Nanomicelles Inhibit Articular Cartilage Deterioration and Reduce Disease Severity in Experimental Inflammatory Arthritis

Akshay Vyawahare, Rehan Khan, et al.

OCTOBER 12, 2022

ACS NANO

READ 🗹

Get More Suggestions >